UCLouvain

École polytechnique de Louvain

Assessing local oceanographic processes that mitigate thermal stress on coral reefs of the Queensland Plateau during the 2024 marine heatwave

Author: **Julien Monfils**
Supervisors: **Emmanuel Hanert, Jonathan Lambrechts, Vincent Legat**
Readers: **Severine Choukroun, Louis Rycx Lamme d'Huisnacht**
Academic year 2025–2026
Master [120] in Mechanical Engineering

Abstract

Coral reef ecosystems are increasingly threatened by climate change and the unprecedented rise in ocean temperature. The growing frequency and intensity of marine heatwaves have led to more severe and widespread coral bleaching events worldwide. During the 2023-2024 global bleaching events, coral reefs around the world were exposed to an intense marine heatwave. Among those, the reefs of the Queensland Plateau were exposed to extreme heat stress but field surveys conducted during the warm season have reported unexpectedly low levels of bleaching across several reefs in the region.

This thesis investigates the oceanic conditions and bleaching patterns associated with this event using SLIM, a three-dimensional baroclinic hydrodynamic model. The objective is to better understand the physical processes that may mitigate thermal stress and contribute to the relative protection of certain reefs within the Queensland Plateau region. The model is validated against in situ observations and Argo float data, demonstrating a consistent representation of the regional thermohaline structure and circulation. Our simulations reproduce the regional hydrodynamics and thermal conditions during the event, and thermal stress accumulation is quantified using the Degree Heating Weeks (DHW) metric derived the modelled temperature fields. Two selected reefs, Lihou and Diamond, are further analyzed in detail to investigate the processes responsible for reduced thermal stress at these locations.

The results reveal strong spatial variability in thermal stress between surface and reef-depth conditions. In particular, some areas exhibit reduced thermal stress at reef depth despite high surface temperature. The analysis highlight the importance of multi-scale processes in modulating thermal stress at reef depth. The southern part of Lihou Reef experiences reduced thermal stress, likely due to large-scale circulation patterns that enhance the presence of cooler and deeper waters. In contrast, Diamond Reef is periodically influenced by cooler water intrusions driven by tidal processes.

These findings emphasise the critical role of local hydrodynamics and subsurface processes in shaping reef thermal environments, and highlight the importance of considering reef-depth conditions when assessing coral reef vulnerability to marine heatwaves.

Acknowledgements

Completing this master thesis has been a rewarding and enriching journey for me.

First and foremost, I would like to express my sincere gratitude to Professor Emmanuel Hanert for his guidance, availability, and kindness throughout this work. His advice and support were invaluable during every stage of this thesis. I am especially grateful for the time he dedicated to answering my questions every weeks, reviewing my work, and coordinating the collaboration with James Cook University. I would also like to thank Jonathan Lambrechts for his participation in the supervision meetings and for his valuable input and feedback throughout this work.

I would also like to warmly thank the entire Slim team — Florian, Amaury, Mattias, Colin, Alexis, Douchan, Théo, Louis, and Miguel — for their support, encouragement, dedication, and the great atmosphere they created throughout the year. Working alongside them has been both professionally enriching and personally rewarding. Their willingness to help, share ideas, and create such a motivating environment made this experience particularly enjoyable. Special thanks go to Miguel for his help with setting up the model and troubleshooting the simulations, and to Louis for generously sharing his knowledge and assisting me with data processing and stress metrics troubleshooting.

I am equally grateful to Stephen Lewis, Séverine Choukroun, and Clothilde Langlais from James Cook University. Their expertise, field knowledge, and insights into the region and coral bleaching phenomena greatly contributed to this work.

I would also like to thank the other master students conducting their thesis under the supervision of Professor Hanert. I truly appreciated the moments we shared together, the discussions, mutual support, and the friendly atmosphere within the group. Their warm welcome at the beginning of the year meant a lot to me, especially as I was coming from another faculty and did not know anyone. Sharing this experience with them greatly contributed to making this year both enjoyable and memorable.

Finally, I would like to express my deepest gratitude to my friends from engineering for all the memorable moments we shared over the years. Their friendship, support, and encouragement made these five years far more enjoyable and helped me overcome the challenges that came along the way. I will always cherish the experiences, discussions, projects, and countless moments we shared together during this important chapter of my life.

Last but not least, I am profoundly thankful to my family for their constant encouragement, patience, and unconditional support throughout my five years of study. They have always been by my side during the most demanding and challenging moments of my academic journey, always believing in me and motivating me to persevere. I would not have reached this stage without their love, trust, and sacrifices, and I am deeply grateful for everything they have done for me.

Use of AI tools Artificial intelligence tools (ChatGPT, Copilot and Claude) were used to assist in improving the clarity, structure, and language of the manuscript. The scientific content, analysis, and conclusions presented in this work were developed entirely by the author. The following approach was followed: each section of the text was first written independently without the use of AI tools. This initial draft was then revised using AI-based assistance, with prompts requesting reformulation into clearer and more formal scientific language. After a critical review of the generated output, selected portions or, in some cases, the entirety of the revised text were incorporated into the manuscript. AI tools were also used to support data processing and the generation of graphical results, enabling more efficient analysis workflows.

Contents

Abstract **3**

Acknowledgements **4**

Contents **6**

List of Figures **8**

List of Acronyms **14**

1 Introduction **15**
1.1 Coral reefs are important ecosystems 15
1.2 Coral reefs are threatened ecosystems 15
1.3 Coral reef refugia can help coral survive bleaching events 16
1.4 Why studying coral reef refugia ? 18
1.5 How to identify coral reef refugia? 19
1.6 Key processes of the GBR refugia. 21
1.6.1 Upwelling. 21
1.6.2 Tidal driven upwelling 22
1.6.3 Eddy drive upwelling 22
1.6.4 Wind driven upwelling 23
1.7 Coral reef refugia on the Queensland Plateau 25
1.8 Objectives of this thesis 26

2 Materials and methods **27**
2.1 Area and time period of interest 27
2.2 The model : SLIM3D 28
2.3 Meshing 32
2.3.1 Slim's mesh structure 32
2.3.2 The final mesh 33
2.4 Bathymetry and forcings 34
2.5 Reef depth MMM computation 35
2.6 DHW computation 37
2.7 Validation 38

3 Results **40**
3.1 Hydrodynamic model validation 40
3.2 Main circulation features 41
3.3 Simulated heat stress 47
3.3.1 Entire Plateau 47

3.3.2 Lihou reef 49
3.3.3 Diamond reef 55

4 Discussion **63**
4.1 Lihou and Diamond reefs exposure to marine heatwaves 63
4.2 Limitations and perspectives 64

5 Conclusion **66**

Bibliography **68**

Appendix A Diamond Reef refigua **74**

Appendix B Analysis of tidal influence on seabed temperature **76**
B.1 Dominant frequency estimation 76
B.2 Tidal signal and seabed temperature 76
B.3 Spectral analysis 77
B.4 Interpretation 77

List of Figures

1 Visual comparison between healthy and bleached coral reefs. Coral bleaching occurs when corals lose their symbiotic algae due to environmental stress, leading to a whitening effect and potential ecosystem degradation. Adapted from [26]. 16

2 Spatial extent and reef-level prevalence of shallow-water (<6 m) coral bleaching during six consecutive mass bleaching events on the GBR. High bleaching prevalence spatially coincides with elevated SST anomaly. Adapted from [40]. 17

3 Projected proportion of thermal refugia and exposed coral reef areas under different global warming scenarios. The number of potential refugia decreases strongly with increasing temperature, suggesting a reduced capacity of coral ecosystems to persist under high-emission pathways. Adapted from [10]. 18

4 Comparison between observed coral bleaching extent and Degree Heating Weeks (DHW) during major marine heatwave events (1998, 2002, 2016). (a) bleaching footprint where the colors represents the following bleaching intensity (dark green : $< 1\%$, light green : $1 - 10\%$, yellow : $10 - 30\%$, orange : $30 - 60\%$, red : $> 60\%$) and (b) DHW map where (blue : $0° - weeks$, red : maximum DHW for each year (respectively 7, 10 and 16 $°C - weeks$)). Higher DHW values correspond closely to increased bleaching severity, confirming DHW as a key thermal stress indicator for coral mortality risk. Adapted from [20]. 20

5 Vertical structure of the ocean water column, illustrating the mixed layer, thermocline, and deep ocean. Strong stratification at the thermocline inhibits vertical mixing. Adapted from [27]. 21

6 Schematic representation of flood tide flow's streamlines in a stratified environment. Strong tidal currents interacting with density stratification can induce vertical circulation patterns and enhance the upward transport of deeper, colder water masses. Adapted from [41]. 22

7 Schematic of eddy-induced pumping in the Capricorn region of the Great Barrier Reef. The interaction between the East Australian Current and bathymetry generates eddies that induce vertical uplift of cold subsurface waters, contributing to local cooling of surface temperatures. Adapted from [44]. 23

8 Long-term mean sea surface temperature (SST) in the Capricorn region showing localized cooling associated with persistent eddy-driven upwelling. Adapted from [44]. 24

9 Wind-driven upwelling induced by Ekman transport. Offshore surface water displacement caused by wind forcing leads to compensatory upward motion of deeper, colder water near the coast, contributing to local cooling of reef environments. Adapted from [33]. 24
10 General overview of the Queensland plateau and its main reefs 25
11 Regional setting of the study area: (a) bathymetric map of the Queensland Plateau and surrounding basins, showing the location of the main coral reef systems. Adapted from [4]; (b) schematic representation of the major surface circulation in the Coral Sea, including the bifurcation of the South Equatorial Current (SEC) and the formation of the East Australian Current (EAC). Adapted from [40] 27
12 Spatial distribution of the studied reefs across the Queensland Plateau overlaid on regional bathymetry. 28
13 Schematic representation of the three-dimensional hydrodynamic domain Ω and its associated boundaries used in SLIM3D. Adapted from [9]. 29
14 Schematic representation of the vertical discretization strategies available in SLIM3D: (a) z-layer coordinates, (b) terrain-following σ-coordinates, and (c) hybrid σ-z coordinates. [42] 33
15 Unstructured two-dimensional computational mesh with local refinement around the Great Barrier Reef and the Queensland Plateau reef systems. 34
16 (a) The three-dimensional computational mesh used in the SLIM3D simulations, based on vertically extruded z-layers. and (b) a schematic of the staircase like discretization of the bathymetry using z-layers 35
17 Vertical distribution of coral cover over the central and northern CSMP, illustrating the variability of coral abundance with depth. Adapted from [18]. 37
18 Example of reef discretization using a regular 500 m spatial grid for local thermal stress assessment. 37
19 Map showing the trajectories of the two Argo floats and the locations of the two ADCP stations used for model validation. The positions of the two vertical transects used in the analysis are also indicated. 39

20 Validation against the southern Argo float, whose trajectory is shown in Fig. 19. Panels (a) and (c) present the vertical salinity and temperature profiles measured by the Argo float and simulated by SLIM on 2023-12-08, respectively. Panels (b) and (d) show the relative mean error over the water column for salinity and temperature, respectively. Overall, low error levels are observed for both variables, demonstrating the model's ability to accurately reproduce the vertical structure of the water column in this region. 42
21 Validation against the northern Argo float, whose trajectory is shown in Fig. 19. Panels (a) and (c) present the vertical salinity and temperature profiles measured by the Argo float and simulated by SLIM on 2023-12-08, respectively. Panels (b) and (d) show the relative mean error over the water column for salinity and temperature, respectively. Overall, low error levels are observed for both variables, demonstrating the model's ability to accurately reproduce the vertical structure of the water column in this region. 43
22 Comparison between modelled and observed seabed temperature time series at the NRSYON station (Fig. 19) over the study period. The model shows good agreement with the *in situ* observations, demonstrating its ability to accurately reproduce the seasonal variability of bottom temperature in this region. 44
23 Comparison between simulated (SLIM) and observed (ADCP) current characteristics at the NRSYON station (Fig. 19) at 8 m depth. (a) Distribution of current velocity magnitude. (b) Directional distribution of currents represented by current roses. These results highlight some inaccuracies in the representation of current direction within the GBR region. 44
24 Comparison between simulated (SLIM) and observed (ADCP) current characteristics at the MYR station (Fig. 19) at 54 m depth. (a) Distribution of current velocity magnitude. (b) Directional distribution of currents represented by current roses. These results show a better representation of the current orientation near the shelf break. 45
25 Mean surface horizontal circulation over the period from December 1, 2023, to April 1, 2024. The main features of the circulation are well captured by the model, namely the South Equatorial Current (SEC), the North Caledonian Jet (NCJ), and the East Australian Current (EAC). 45

26 Mean horizontal circulation over the Queensland Plateau at (a) the surface and (b) 60 m deep during the period from January 1 to May 1, 2024. While the surface circulation is predominantly unidirectional, the flow at depth becomes considerably more complex due to interactions with the reef system, generating localized vorticity and enhanced current velocities in several regions. 46
27 Mean vertical transects of (a) temperature and (b) current velocity during the period from November 2023 to June 2024, along transect A. These plots highlight the strong stratification of the water column in the Coral Sea, as well as the surface currents flowing along both sides of the Queensland Plateau. 48
28 Comparison between (a) maximum simulated surface DHW and (b) the NOAA Coral Reef Watch 5 km Degree Heating Week Annual Maximum (V3.1) for 2024. Adapted from [31]. This figure highlights that, in general, the simulated thermal stress is lower than the satellite-derived estimates. 50
29 Difference between maximum DHW values at the surface and at reef depth over the Queensland Plateau reefs. This figure highlights that some reefs exhibit locally lower DHW values at depth, whereas others show higher thermal stress at depth than at the surface. 51
30 Map of maximum (a) surface DHW, (b) reef-depth DHW, and (c) their difference over Lihou Reef during the period from January 1 to May 1, 2024. The reef is generally experiencing lower thermal stress in the southern region. The reef depth thermal stress is higher than the surface thermal stress over the whole reef. 51
31 South-central Lihou Reef (depth: 5 m). Temporal evolution of temperature and cumulative thermal stress (DHW) at the surface and at reef depth during the study period. These plots show a very small temperature difference between the surface and reef depth, leading to increased thermal stress at depth due to the lower MMM. 52
32 North-central Lihou Reef (depth: 18 m). Temporal evolution of temperature and cumulative thermal stress (DHW) at the surface and at reef depth during the study period. These time series show a clear temperature difference between surface and depth; However, this gradient is not sufficient to reduce thermal stress due to the lower MMM at reef depth, resulting in higher DHW values at depth. 53

33 (a) Mean Sea Surface Temperature (SST) and (b) vertical velocity over Lihou Reef during the period from 2024-01-01 to 2024-05-01. The SST field shows lower temperatures in the southern part of the reef and within the lagoon compared to surrounding waters, while the vertical velocity field highlights areas of upward motion (positive values) indicative of localized upwelling across the reef system. For clarity, the color scale of vertical velocity is restricted to positive values. 54
34 Mean horizontal circulation at 60 m deep around Lihou Reef during the period from January 1 to May 1, 2024. This figure highlights the portion of the NCJ current deflected by Marion Reef and directed toward the southern part of Lihou Reef at relatively high velocity forming a large eddy (indicated by the arrow). 54
35 (a) Mean temperature and (b) mean vertical velocity at 60 m depth during the period from January 1 to May 1, 2024. This figure highlights a cold region associated with upwelling induced by eddy pumping linked to the large eddy generated by the NCJ current (indicated by the arrow). 55
36 Mean vertical transect of (a) temperature and (b) vertical velocity during the period from January 1 to May 1, 2024 along transect B (Fig. 19). This figure highlights cold-water upwelling along the southern part of the reef. The temperature colorbar is restricted to a narrow range to better emphasize the cold water advected over the southern reef. The southern part of the reef is denoted by S and the northern part by N. . 56
37 Map of maximum (a) surface DHW, (b) reef-depth DHW, and (c) their difference over Diamond Reef during the period from January 1 to May 1, 2024. The reef exhibits strong spatial variability at depth, with some areas showing high surface thermal stress (>8 DHW) while remaining weakly affected at depth (<4 DHW). 57
38 South-central Diamond Reef (depth: 40 m). Temporal evolution of temperature and cumulative thermal stress (DHW) at the surface and at reef depth during the study period. These time series show reduced temperature variability and lower warming amplitude at depth compared to the surface, resulting in delayed exceedance of the bleaching threshold and reduced DHW accumulation. 58
39 North-eastern exposed region of Diamond Reef (depth: 5.5 m). Temporal evolution of temperature and cumulative thermal stress (DHW) at the surface and at reef depth during the study period. These time series show weak vertical temperature differences, leading to early and prolonged exceedance of the bleaching threshold at depth and high DHW accumulation. 58

40 Mean (a) temperature, (b) vertical velocity, and (c) horizontal current velocity at 40 m depth near Diamond Reef during the period from January 1 to May 1, 2024. Ovals indicate regions of divergent streamlines and positive vertical velocities, while rectangles highlight areas of fast-flowing currents. For clarity, the colormap of vertical velocity is restricted to positive values. 59
41 Vertical profile time series of (a) temperature and (b) current direction at the southern refugium (Fig. 37) during the period from January 1 to May 1, 2024. These figures highlight the intrusion of cold water into the Diamond lagoon following a 12-hour cycle linked to the tidal regime in this area. 61
42 Vertical profile time series of (a) temperature and (b) current direction at the north-eastern exposed region (Fig. 37) during the period from January 1 to May 1, 2024. These figures highlight weak vertical temperature differences in this region and the absence of cold-water intrusion driven by tides. 62
43 Vertical profile time series of (a) temperature and (b) current direction at the northern refugium (Fig. 37) during the period from January 1 to May 1, 2024. These figures highlight the intrusion of cold water into the Diamond lagoon following a 12-hour cycle linked to the tidal regime in this area. 74
44 Vertical profile time series of (a) temperature and (b) current direction at the eastern refugium (Fig. 37) during the period from January 1 to May 1, 2024. These figures highlight the intrusion of cold water into the Diamond lagoon following a 12-hour cycle linked to the tidal regime in this area. 75

List of Acronyms

ADCP	Acoustic Doppler Current Profiler.
B	Local climatological Bias between the SST and the seabed temperature.
CSIRO	Commonwealth Scientific and Industrial Research Organisation.
CSMP	Coral Sea Marine Park.
DHW	Degree Heating Week.
EAC	East Australian Current.
GBR	Great Barrier Reef.
GBRMP	Great Barrier Marine Park.
HS	HotSpot.
MMM	Maximum Monthly Mean.
NCJ	North Caledonian Jet.
NOAA	National Oceanic and Atmospheric Administration.
RMSE	Root Mean Square Error.
SEC	South Equatorial Current.
SLIM	Second-generation Louvain-la-Neuve Ice-ocean Model.
SSS	Sea Surface Salinity.
SST	Sea Surface Temperature.

1 Introduction

1.1 Coral reefs are important ecosystems

Coral reefs cover only 0.1 to 0.5% of the ocean floor [28]. However, the coral reef ecosystems are very rich and diverse [34]. In fact, they are hotspots of biodiversity for a multitude of organisms that use them as spawning, nursery, breeding and feeding areas [28]. Reef building corals also help other ecosystems to thrive by protecting them from currents, waves, storms and more generally by reducing shoreline erosion. They further participate in the creation of favourable conditions for the growth of mangroves and seagrass ecosystems [28]. Coral reefs are able to fix high quantities of Nitrogen in nutrient poor environments. Fixing Nitrogen helps the reef enhance its own productivity, but also increases the productivity of adjacent pelagic communities [28].

The Great Barrier Reef (GBR) is the most extensive coral reef and covers an area of $348\,000\,\mathrm{km}^2$ [15]. It is situated at a few tens of kilometres of the Queensland's coasts. In average, the economic value of coral reefs ecosystems over the world was estimated at 352.000 \$/ha/year in 2011 [8]. This high economic value is explained by their storm and erosion protection capacities and their abilities to attract tourists. Coral reef ecosystems also contribute to local fisheries by enhancing seafood and fish catches [28].

1.2 Coral reefs are threatened ecosystems

Corals are often associated with photo-symbiotic unicellular algae called zooxanthellae. These algae live in symbiosis with the coral within its tissues. The advantage of symbiosis comes from the exchange in nutritional resources between the algae that can photosynthesise and the coral that can provide carbon to the algae. These fluxes allow the corals and thus the reefs to survive in water with low concentration of Nitrogen and Phosphorus [39]. This symbiosis enables the coral to grow its skeleton much faster which helps it building the reef faster than external forces can erode it [29].

In 2025, the GBR has experienced its sixth mass bleaching event since 2016 [45]. The bleaching phenomenon consists of the loss of colour caused by the partial or total diminution of zooxanthellae in the coral's cells (Fig. 1) [11]. For the majority of corals, as their tissues are not heavily pigmented, their flesh is transparent or translucent and thus only their white calcium carbonate skeleton can be seen [11]. Bleaching is a natural phenomenon and displays seasonal variations. In fact, the main factors impacting coral bleaching are changes in the water temperature [25], but bleaching can also be caused by changes in water salinity, pollution and light exposure [17]. The increase



Figure 1: Visual comparison between healthy and bleached coral reefs. Coral bleaching occurs when corals lose their symbiotic algae due to environmental stress, leading to a whitening effect and potential ecosystem degradation. Adapted from [26].

in frequency of mass bleaching event can be explained by the rise of the Sea Surface Temperature (SST) measured around coral reefs and caused by global warming [17]. The zooxanthellae and the corals are not able to adapt fast enough to this warming [17]. The consequence of these mass bleaching events is an important mortality of the corals. The higher the temperature and the longer the warm period, the higher the mortality rate will be [17].

1.3 Coral reef refugia can help coral survive bleaching events

For all the reasons mentioned before, it is important to take actions to help these ecosystems survive. Some studies highlight the presence of thermal refugia, which are relatively stable and resilient habitat where the corals can live and then expand back in the rest of the ocean when the stresses are lower. These refugia are generally experiencing lower bleaching footprint than the rest of the reefs during all marine heatwaves. These refugia are often found at regions in which the sea surface temperature is significantly cooler than the surrounding water [40]. This is explained by the fact that the temperature is the main stressor causing the bleaching of corals.

The high bleaching footprint is correlated with the high SST anomaly (Fig. 2). The first refugium is situated in the Southern GBR at the outer shelf edge off the Pompeys to the Swains complexes. The second refugium is situated in the North along the outer shelf from Torres Strait to the ribbon reefs off Cape York [40]. These refugia are generally present in areas with favourable oceanographic or meteorological processes [40]. These phenomena provide regular upwelling that brings cold water from the depth to

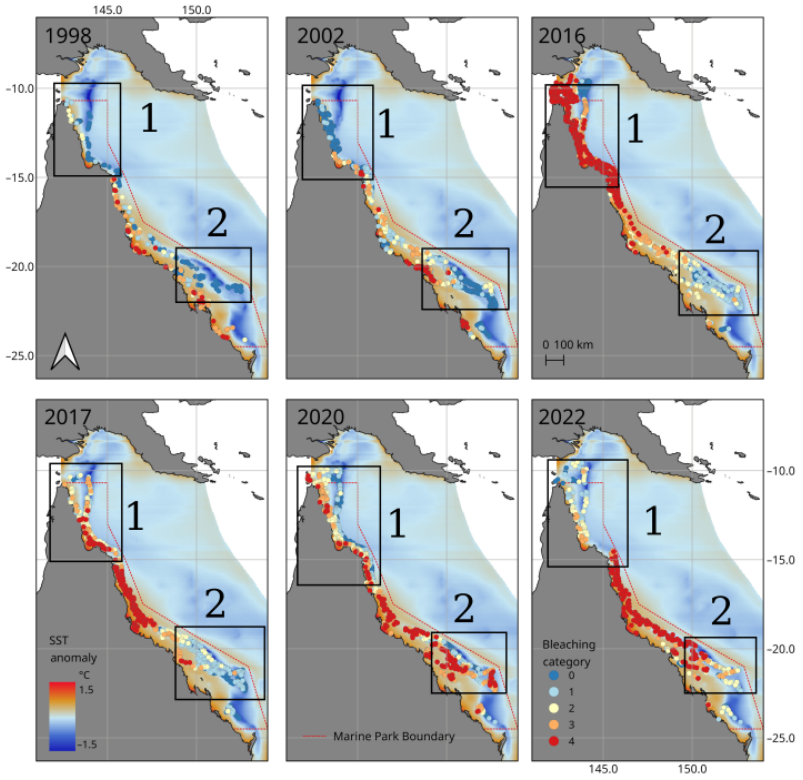


Figure 2: Spatial extent and reef-level prevalence of shallow-water (<6 m) coral bleaching during six consecutive mass bleaching events on the GBR. High bleaching prevalence spatially coincides with elevated SST anomaly. Adapted from [40].

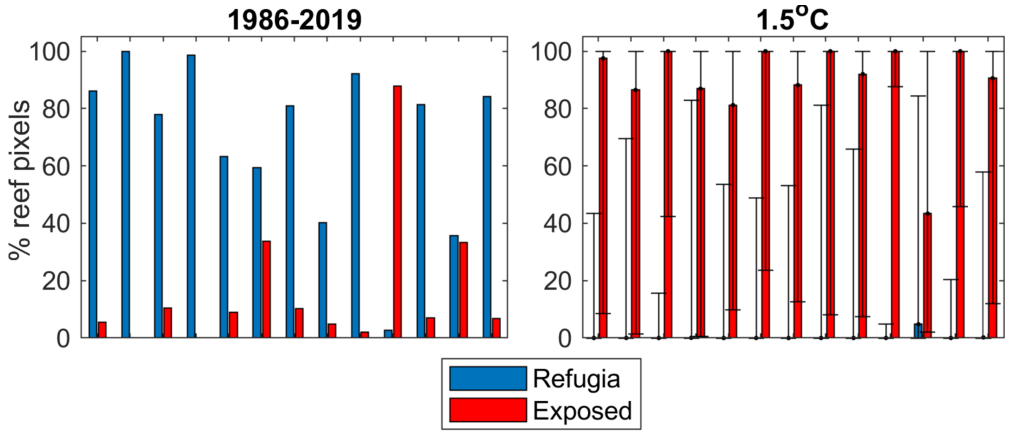


Figure 3: Projected proportion of thermal refugia and exposed coral reef areas under different global warming scenarios. The number of potential refugia decreases strongly with increasing temperature, suggesting a reduced capacity of coral ecosystems to persist under high-emission pathways. Adapted from [10].

the surface, reducing the temperature at the reefs depth. These processes are multiple; complex topography interacting with tidal currents, upwelling favourable winds, cyclonic eddies and internal waves [40].

1.4 Why studying coral reef refugia ?

The understanding of the complex oceanographic phenomena involved in the circulation across the GBR and, more generally, in the Coral Sea is important for informing coral reef conservation decisions. In their study, Weeks et al. argue that establishing protected areas in regions with a high probability of coral bleaching and mass mortality may not be the most effective strategy for sustaining coral populations. Instead, they suggest prioritising the protection of potential refugia that could persist under future ocean warming, thereby increasing the chances of coral species survival [44].

Furthermore, some studies show that these refugia might survive the global warming [40], but other scientists are less optimistic about the future of coral reefs.Dixon et al [10] have shown that a lot of reefs were considered as refugia in the 1986-2019 climate (Fig. 3). But this number decrease depending on the global warming scenario considered. For a warming above $1.5°C$, very few refugia can still support living corals. Nevertheless, these studies use relatively coarse models that do not take into account the local phenomena on small spatial scales such as the interaction between local currents patterns and the bathymetry of the reef. It is a major gap in the research considering the future of coral reef refugia.

1.5 How to identify coral reef refugia?

Because coral bleaching depends on both temperature and thermal stress duration, only relying on the SST is not an optimal criterion. A more common criterion used to predict coral bleaching is the Degree Heating Week (DHW). This criterion integrates both the amplitude of the heat stress and the duration of this stress.

To define the DHW, we first need to introduce the HotSpot (HS) metric, which measures the intensity of the instantaneous heat stress. It is defined as follows :

$$HS\ [^{\circ}\mathrm{C}] = \begin{cases} 0 & \text{if } SST \leq MMM \\ SST - MMM & \text{if } SST > MMM \end{cases}$$

where Maximum Monthly Mean (MMM) is the Maximum Monthly Mean, a climatological measure that uses at each location, the warmest of the 12 climatological monthly mean temperatures [24].

The DHW is then defined as the running sum of all hotspots on a 12 weeks period (84 days) above a certain threshold often taken as $1°C$ [23]. It can be written as :

$$DHW\ [^{\circ}\mathrm{C} - \mathrm{week}] = \frac{1}{7}\sum_{i=1}^{84} HS_i \text{ when } HS_i \geq 1\,^{\circ}\mathrm{C}$$

It is then possible to use different thresholds on the DHW metrics to predict mass bleaching and mass mortality of the corals. $4°C - weeks$ is often used as a threshold for the onset of mass bleaching while $8°C - weeks$ is used for the onset of mass mortality [12].

Fig. 4a shows the footprint of bleaching measured by aerial surveys which represents the fraction of the corals bleached. Going from dark green ($< 1\%$), to red ($> 60\%$). Fig. 4b shows the DHW map corresponding to the same bleaching event. As we can see, the places with the highest bleaching footprint are the places with the highest DHW values.

The main limitation to this metric is that it uses the ocean temperature at the surface while the corals are not always close to the surface. The temperature is generally lower at reef depth than at the surface and the DHW computed with the surface temperature could hence overestimate bleaching. For example, the satellite measurements of the SST used by the National Oceanic and Atmospheric Administration (NOAA) represents the temperature of the first $10\mu m$ of the water column [22]. It might thus be interesting to compute the DHW metric using the temperature at the depth of the coral reefs.

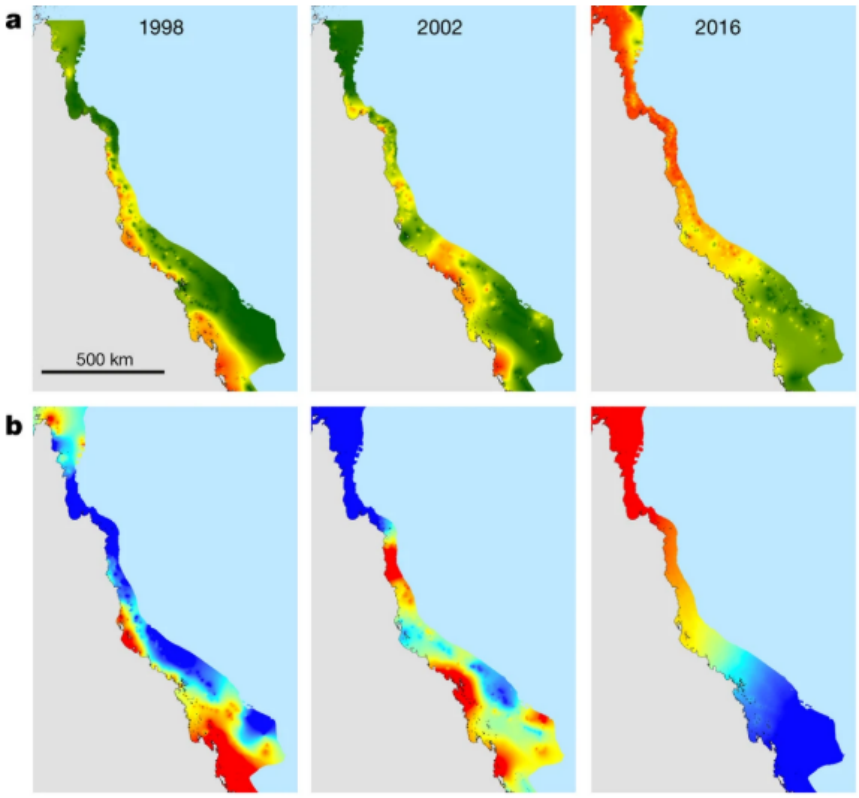


Figure 4: Comparison between observed coral bleaching extent and Degree Heating Weeks (DHW) during major marine heatwave events (1998, 2002, 2016). (a) bleaching footprint where the colors represents the following bleaching intensity (dark green : $< 1\%$, light green : $1 - 10\%$, yellow : $10 - 30\%$, orange : $30 - 60\%$, red : $> 60\%$) and (b) DHW map where (blue : $0° - weeks$, red : maximum DHW for each year (respectively 7, 10 and 16 $°C - weeks$)). Higher DHW values correspond closely to increased bleaching severity, confirming DHW as a key thermal stress indicator for coral mortality risk. Adapted from [20].

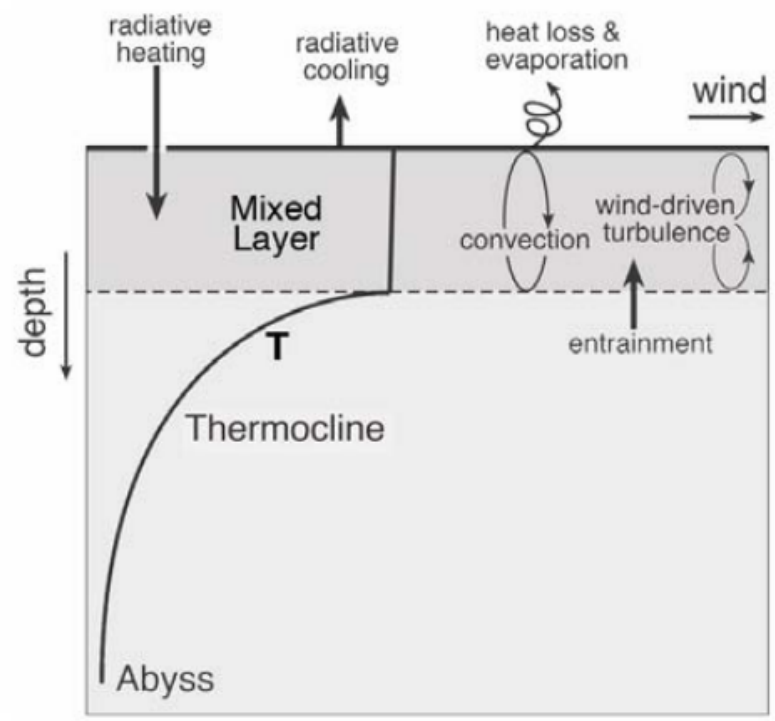


Figure 5: Vertical structure of the ocean water column, illustrating the mixed layer, thermocline, and deep ocean. Strong stratification at the thermocline inhibits vertical mixing. Adapted from [27].

1.6 Key processes of the GBR refugia.

1.6.1 Upwelling.

As explained before, the main factor leading to refugia, is the upwelling of deep cold water [40]. The ocean being generally stratified, cold dense water will lie below warmer water at reef depth in the mixed layer. (Fig. 5). The mixed layer corresponds to the part of the water column where turbulent motion of the water leads to uniform temperature and salinity. Below this mixed layer is the thermocline. It is a region with rapid variations of the water temperature and salinity, implying a rapid increase in water density. This thermocline is present to match the properties of the two different water masses, the light mixed layer and the cold abyssal water. Because in the thermocline, density is increasing rapidly over depth, it makes this part of the water column very stable [27] and thus impede transfer of cold water to the surface. There are many different processes that are able to bring cold water from below the thermocline despite the resistance caused by stratification. A few of them will be presented in this section.

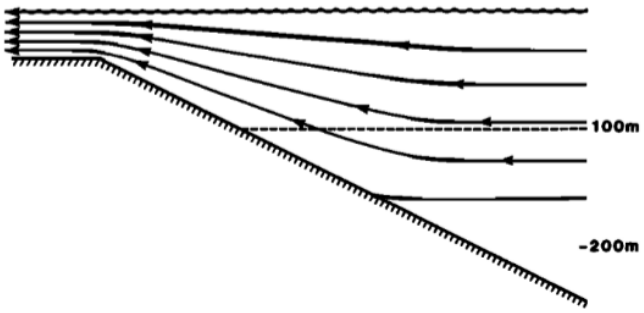


Figure 6: Schematic representation of flood tide flow's streamlines in a stratified environment. Strong tidal currents interacting with density stratification can induce vertical circulation patterns and enhance the upward transport of deeper, colder water masses. Adapted from [41].

1.6.2 Tidal driven upwelling

The GBR is subject to vigorous tides and tidal currents. In some particular places, as the reef gets very dense, the tidal current is concentrated in the narrow passages between the reefs which can create high velocity tidal flows. The water in the first 100m of depth is well mixed. But below that depth, the temperature and salinity highly varies with depth. During the flood tide, the water comes uniformly from all directions. But because of stratification, the water from below the thermocline resists being pulled up. The resulting flow has a shape shown in Fig. 6.

Thompson and Golding[41] state that at any given time, there is a maximum internal wave speed. If the flow is at velocity higher than this maximum speed, its called supercritical and no internal waves caused by stratification can exist. This implies that there can be no vertical velocity shear caused by stratification. Hence, the flow at the bottom must be forward and cold water from below the mixed layer down to a certain depth will be sucked up during the flood tide.

1.6.3 Eddy drive upwelling

Eddies can be source of upwelling or downwelling. This phenomenon is called *eddy pumping*. In the case of the GBR, Weeks et al. [44] have shown that the strong East Australian Current (EAC) is flowing along the coast southward. Because of the friction caused by the shallowing sea floor and the coast nearby, the flow near the coast is slowed down creating a velocity shear. Because of the bathymetry of the continental shelf, a large eddy of 150 km of diameter is created near the Capricorn channel (Fig. 7a).

Because of the Coriolis effect, the water inside the eddy is subjected to a centrifugal fictive force resulting in a net outgoing mass flux of water on the horizontal plane, which creates a depletion of the sea surface level (Fig. 7b). To balance this outgoing mass flux, deep water must be transported upward. When this water mixes with the surface

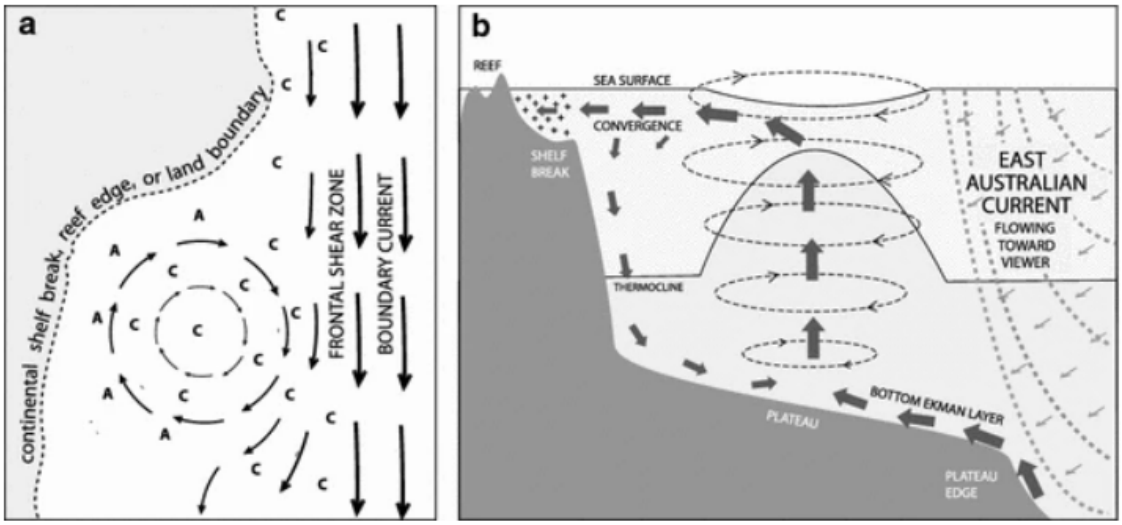


Figure 7: Schematic of eddy-induced pumping in the Capricorn region of the Great Barrier Reef. The interaction between the East Australian Current and bathymetry generates eddies that induce vertical uplift of cold subsurface waters, contributing to local cooling of surface temperatures. Adapted from [44].

water, it lowers the SST.

As shown in Fig. 8, the mean SST is smaller downstream from the Capricorn eddy, indicating an important and reliable source of cold water upwelling.

1.6.4 Wind driven upwelling

Upwelling can also be driven by winds. It has been observed that these types of upwelling happens on a variety of time scales and frequency. High frequency and small scale upwelling events are relatively frequent and are mostly responsible for the chemical properties of the water surrounding the shelf break [2]. On the other hand, less frequent but larger scale, low frequency water intrusion penetrates through the reef matrix. The time scale of these phenomena is of the order of magnitude of 1 to 4 weeks and the spatial scale is around 50 to 100 km. These events are predominant in the season between October and April. These events are strongly coupled with southward reversal or extended relaxations of the south-easterly trade winds which happens more often during the summer [2].

The physics of these intrusions events implies that it can be in a first approximation explained by purely barotropic theory. In fact, during the trade winds reversal events, because of the Ekman transport, the water in the upper layer (the Ekman layer) is transported towards the East, meaning that the water goes offshore. Because of this mass flux going offshore, water has to come from the depth to get a balance, creating upwelling of cold water from the depth near the coast (Fig. 9).

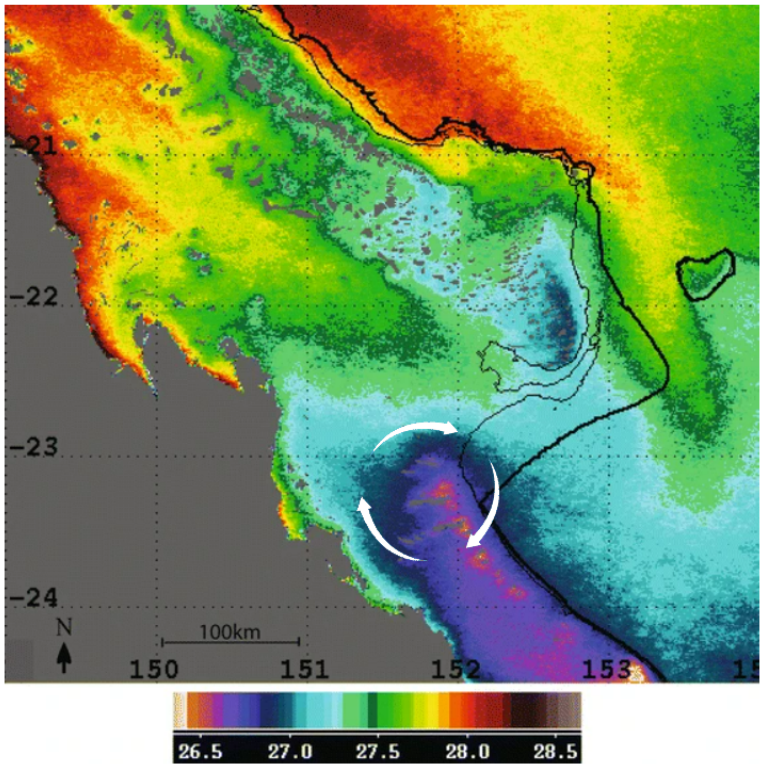


Figure 8: Long-term mean sea surface temperature (SST) in the Capricorn region showing localized cooling associated with persistent eddy-driven upwelling. Adapted from [44].

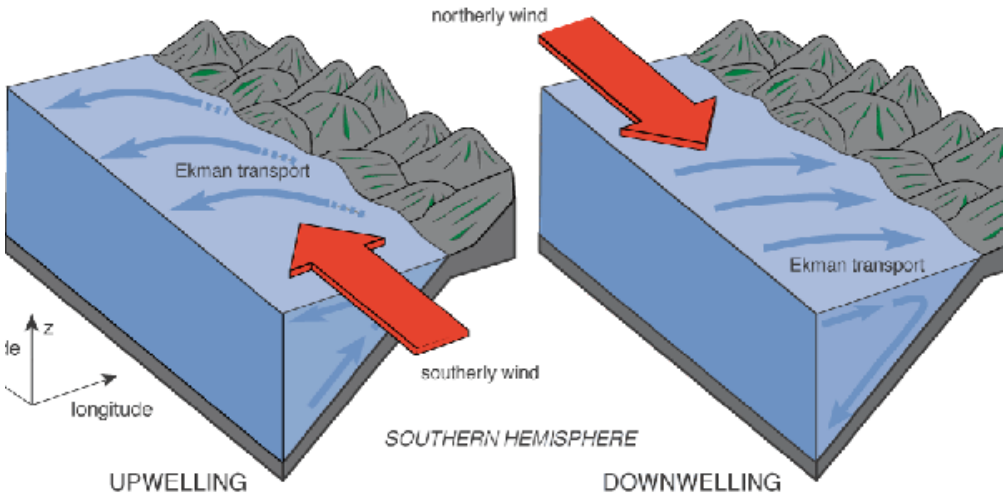


Figure 9: Wind-driven upwelling induced by Ekman transport. Offshore surface water displacement caused by wind forcing leads to compensatory upward motion of deeper, colder water near the coast, contributing to local cooling of reef environments. Adapted from [33].

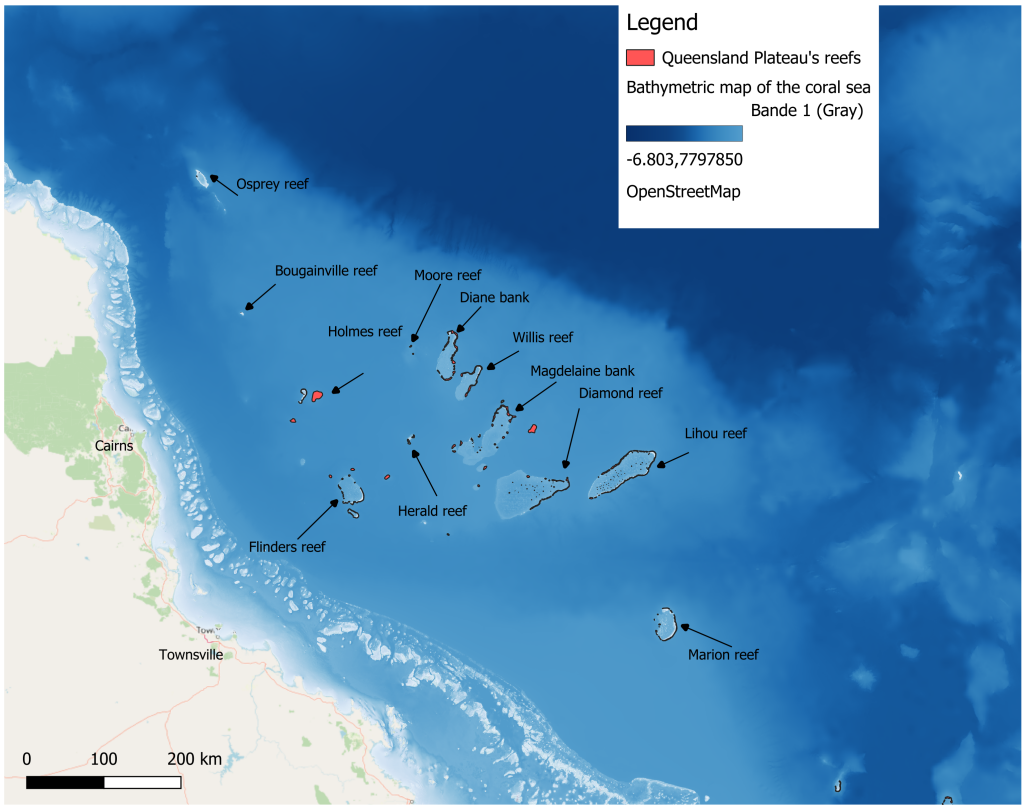


Figure 10: General overview of the Queensland plateau and its main reefs

1.7 Coral reef refugia on the Queensland Plateau

Coral climate refugia in the GBR have been the subject of a lot of studies in the recent years. The coral reefs situated on the Queensland Plateau haven't been studied yet under the refugia perspective. The Queensland Plateau is situated between the GBR and the Coral Sea and has a length of approximately 500 km. The reefs present on this Plateau are not part of the Great Barrier Marine Park (GBRMP), but they are protected at different levels (National Park IUCN II, habitat protection zone IUCN IV) [1].

According to the report on the health of coral reef, different reefs have been previously identified as bright spots in terms of coral cover, richness and fish biomass. This include the Ashmore, Boot, Bougainville, Mellish and Moore reefs. Five reefs in the centre Coral Sea Marine Park (CSMP) had a very low ($< 10\%$) coral cover during the during the observations (Marion Reef : 5.9%, Lihou Reef : 6.0%, Diamond Islets : 7.0%, Herald cays : 7.5% and Willis Islets : 8.9%). Low to moderate levels of bleaching were observed during this campaign. Though, this campaign was conducted before the marine heatwave had reached its peak in late March with large areas of the CSMP exposed to DHW higher than 12 and up to 17 DHW [18].

But more recent surveys estimates that the important marine heatwave of 2024 has caused very low level of bleaching driven mortality on four of the reefs monitored

(Willis, Herald, Diamond and Lihou) despite the very high heat stress (up to 16 DHW) [19]. A limitation of this study is that the surveyed reefs had a very low coral coverage (around 10%), thus more sensitive coral taxa where already dead because of previous bleaching event.

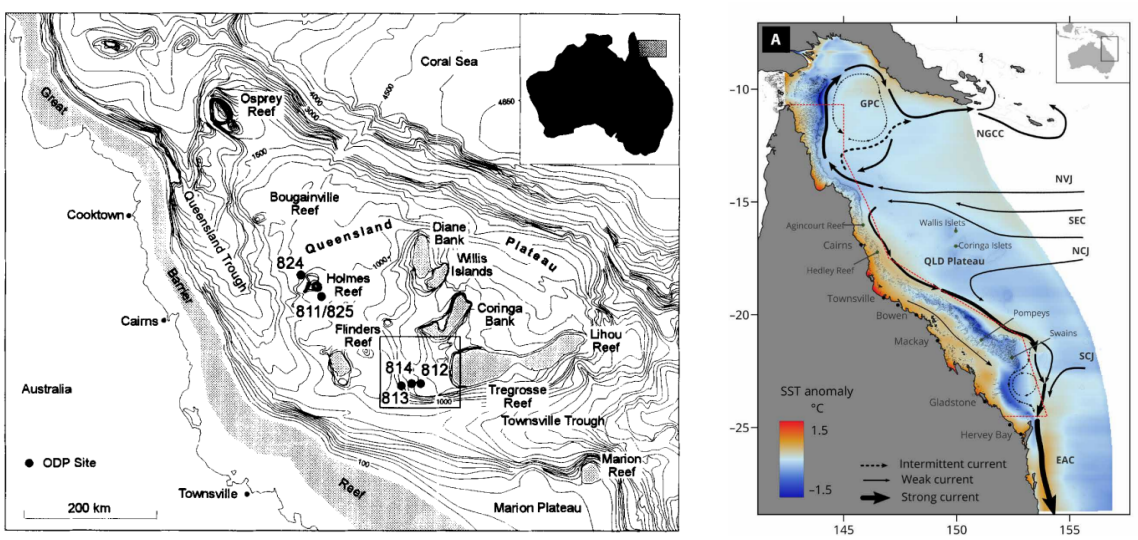
1.8 Objectives of this thesis

The objective of this thesis is to simulate the ocean dynamics in the vicinity of the Queensland Plateau during the 2024 marine heatwave to identify the local oceanographic drivers that could lead to the presence of climate refugia on the Queensland Plateau.

We will first try to replicate the thermal stress patterns observed during the 2023-2024 marine heat wave on the Queensland Plateau in order to evaluate the impacts of the different parameters that influence the oceanographical processes in these areas (bathymetry, currents, winds, ...)

The main research question that will assess this master thesis is : *"What are the local oceanographic drivers protecting reefs on the Queensland Plateau during the 2023 - 2024 marine heatwave ?"*

To do so, the simulations will be realised using the Second-generation Louvain-la-Neuve Ice-ocean Model (SLIM)[36], a 3D hydrodynamic model developped at UCLouvain. The temporal domain of the simulation will be from September 2023 to February 2024 in order to capture the whole marine heatwave. This model will take into account various factors such as the complex bathymetry of the coral reefs, the winds and the currents. The data obtained from this model include the velocity vector field, the temperature and other important oceanographical data that will be used to analyse the physics of the processes leading or not to bleaching of the corals during hyperthermal events. This model is able to compute these data on a very fine grid, enabling the analysis of complex phenomena on very small local scale.



(a) (b)

Figure 11: Regional setting of the study area: (a) bathymetric map of the Queensland Plateau and surrounding basins, showing the location of the main coral reef systems. Adapted from [4]; (b) schematic representation of the major surface circulation in the Coral Sea, including the bifurcation of the South Equatorial Current (SEC) and the formation of the East Australian Current (EAC). Adapted from [40]

2 Materials and methods

2.1 Area and time period of interest

The Queensland Plateau is located offshore of northeastern Australia in the Coral Sea. It is bounded by the Queensland Trough to the west, the Townsville Trough to the south, and the Coral Sea Basin to the north and east (Fig. 11a). The average depth of the Queensland Plateau is approximately 1000 m [4], which is significantly shallower than the surrounding Coral Sea Basin, where depth reach approximately 4500 m. These two regions are connected by steep bathymetric slopes (Fig. 11a). The large-scale circulation in the coral Sea is primarily driven by the South Equatorial Current (SEC), which bifurcates into several branches upon reaching the western Coral Sea. Around 17 °S, the SEC separates into an equatorward branch and a poleward branch flowing along the GBR, contributing to the formation of the EAC (Fig. 11b). The prevailing winds over the GBR region are the southeasterly trade winds. However, during some years, the Australian monsoon fails to fully develop, which can lead to a reversal of the dominant wind regime, with northwesterly winds replacing the southeasterlies [2]. The reef systems investigated in this study are distributed across the Queensland Plateau and are shown in Fig. 12.

The objective of this study is to investigate the coral bleaching patterns associated with the austral summer marine heatwave of 2023–2024. Observations collected dur-

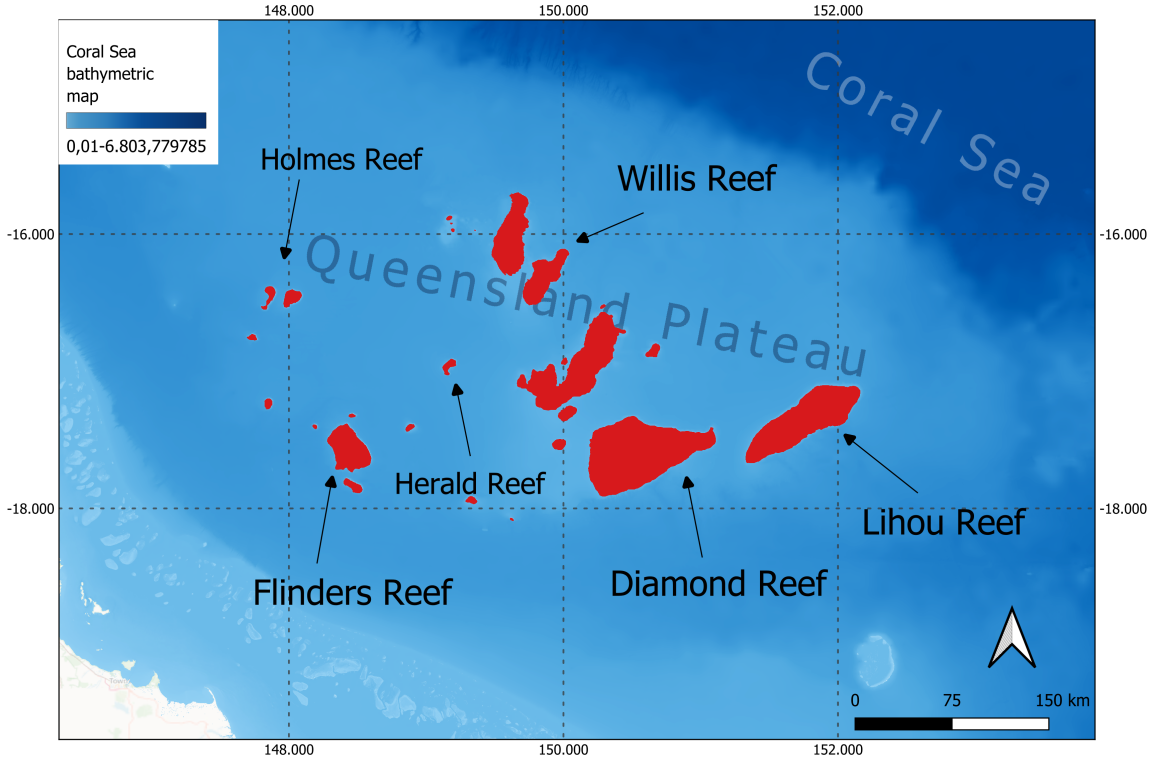


Figure 12: Spatial distribution of the studied reefs across the Queensland Plateau overlaid on regional bathymetry.

ing the CSMP Coral Reef Health Surveys of 2023 and 2024 identified reefs such as Bougainville reef and Moore Reef as potential thermal refugia [18]. Additional reefs, including Lihou, Diamond, Herald and Willis Reefs, exhibited an increase in coral cover between February 2023 and July 2024 [19]. During this marine heatwave event, thermal stress peaked in late March 2024, with some regions experiencing values exceeding 16 DHW [19]. To capture the period associated with the highest thermal stress on coral ecosystems, the simulation period extends from June 2023 to early June 2024. Starting the simulation several months before the peak heat stress period allows the model spin-up phase to occur prior to the main period of interest, namely January to April 2024.

2.2 The model : SLIM3D

To investigate the hydrodynamic processes controlling the thermal environment of the Queensland Plateau reefs during the 2023–2024 marine heatwave, a three-dimensional hydrodynamic model is required. In particular, the study aims to resolve the interaction between large-scale circulation, local bathymetry, vertical stratification and reef-scale thermal variability, all of which may influence the spatial distribution of heat stress across the reef systems.

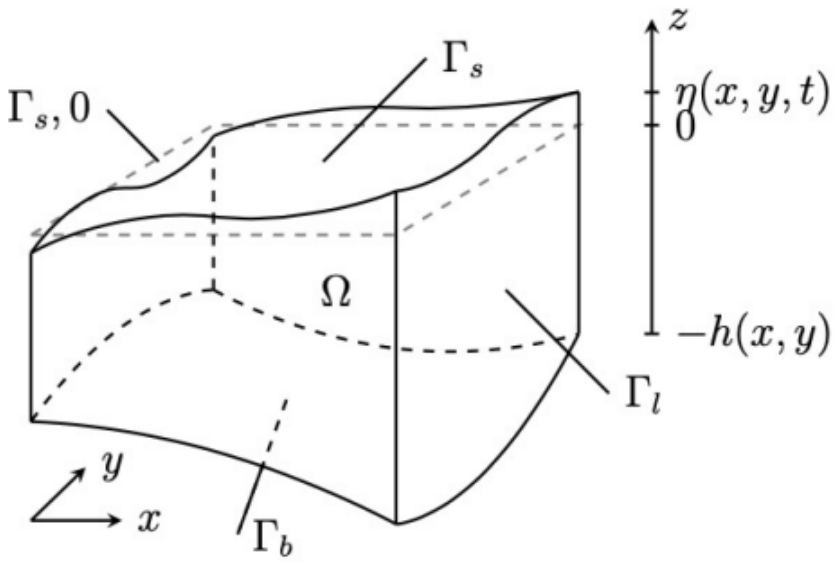


Figure 13: Schematic representation of the three-dimensional hydrodynamic domain Ω and its associated boundaries used in SLIM3D. Adapted from [9].

For this purpose, the SLIM3D hydrodynamic model, developed at UCLouvain, is employed. SLIM3D is a finite-element ocean model based on unstructured meshes, allowing for variable spatial resolution across the computational domain. This approach is particularly well suited for the present study, as it enables high resolution over the reefs of interest while maintaining a reasonable computational cost over the larger Coral Sea domain. SLIM3D solves the three-dimensional hydrostatic equations governing geophysical flows and includes the transport of tracers such as temperature and salinity. The model also accounts for atmospheric forcing, turbulent mixing processes and free-surface dynamics, making it suitable for simulating the physical processes associated with marine heatwaves and reef-scale thermal variability. The following sections present the governing equations of the model, the numerical discretization strategy, the mesh structure and the physical parameterizations used in this study.

The domain Ω (Fig. 13) is characterized by three dimensions : x and y represents the horizontal dimensions of a local planar projection of the Earth's surface while z is the verical coordinate [13]. The domain is bounded by three types of boundaries : The fixed lateral boundaries (Γ_l), the fixed bottom boundary (Γ_b) corresponding to the sea floor ($z = -h(x, y)$ where $h(x, y)$ is the bathymetry) and the moving top surface boundary (Γ_s) following the sea surface elevation ($z = \eta(x, y, t)$ where $\eta(x, y, t)$ is the sea surface elevation defined with respect to a reference surface layer $\Gamma_{s,0}$ corresponding to a sea at rest).

The model accounts for five governing equations, namely the momentum, continuity, and tracer equations. It computes several prognostic and diagnostic variables, including

the horizontal velocity field $\mathbf{u}(t, \mathbf{x})$ (in $\mathrm{m\,s^{-1}}$), the vertical velocity component $w(t, \mathbf{x})$ (in $\mathrm{m\,s^{-1}}$), and the sea surface elevation $\eta(t, x, y)$ (in m). It also simulates salinity $S(t, \mathbf{x})$ (in $\mathrm{g\,kg^{-1}}$) and temperature $T(t, \mathbf{x})$ (in °C), as well as hydrostatic pressure $p(t, \mathbf{x})$ (in $\mathrm{Nm^{-2}}$). Finally, the model provides the density deviation from a reference state, denoted $\rho'(t, \mathbf{x})$, expressed in $\mathrm{kgm^{-3}}$.

Two main assumptions are made to simplify the equations of the model; The hydrostatic hypothesis and the Boussinesq approximation [13]. The hydrostatic hypothesis states that the gravity applied on the water column is compensated by the vertical pressure gradient. Mathematically, the vertical momentum conservation equation reduces to :

$$\frac{\partial p}{\partial z} = -\rho g$$

with g being the gravitational acceleration and $\rho(t, \mathbf{x})$ the water density. The Boussinesq approximation states that the density variation is much smaller than the reference density ($\rho - \rho_0 \ll \rho$). Hence, the density variation can be neglected in all terms of the momentum equation expect for the gravity term.

With these two assumptions, the momentum, continuity and sea surface equations becomes :

$$\begin{aligned}
\frac{\partial \mathbf{u}}{\partial t} + \nabla_h \cdot (\mathbf{u}\mathbf{u}) + \frac{\partial (w\mathbf{u})}{\partial z} &= \nabla_h \cdot (\nu_h \nabla_h \mathbf{u}) + \frac{\partial}{\partial z}\left(\nu \frac{\partial \mathbf{u}}{\partial z}\right) - f\hat{\mathbf{e}}_z \times \mathbf{u} - \frac{1}{\rho_0}\nabla_h p \\
\frac{\partial w}{\partial z} &= -\nabla_h \cdot \mathbf{u} \\
\frac{\partial \eta}{\partial t} &= -\nabla_h \cdot \int_{-h}^{\eta} \mathbf{u}\, dz
\end{aligned}$$

Where $\nabla_h = \left(\frac{\partial}{\partial x}, \frac{\partial}{\partial y}\right)$is the horizontal gradient operator, f is the Coriolis factor, $\hat{\mathbf{e}}_z$ is the upward vertical unit vector, ν_h and ν are the horizontal and vertical eddy viscosities.

The ocean pressure gradient is influenced by the atmospheric pressure. This can be seen by decomposing the pressure gradient as follows :

$$\frac{1}{\rho_0}\nabla_h p = \frac{1}{\rho_0}\nabla_h p_{atm} + g\nabla_h \eta + \frac{g}{\rho_0}\nabla_h \int_z^{\eta} \rho'\, dz'$$

where p_{atm} is the atmospheric pressure and ρ' is a function of S and T and is computed from the equation of state of sea water described in Jackett et al. (2006) [21]. Both temperature and salinity are computed as tracers and modeled using advection-diffusion equations. For a generic tracer C, the equation reads :

$$\frac{\partial C}{\partial t} + \nabla_h \cdot (\mathbf{u}C) + \frac{\partial (wC)}{\partial z} = \nabla_h \cdot (k_h \nabla_h C) + \frac{\partial}{\partial z}\left(k \frac{\partial C}{\partial z}\right)$$

Where k_h and k are the horizontal and vertical diffusivities of the tracer C. To include subscale turbulent processes that are not resolved because of the grid size, a turbulent closure model is needed. These processes are taken into account by using the turbulent variables ν_h, ν, k_h and k. ν_h follows the Smagorinsky closure scheme [37] while k_h is parametrised following Okubo's approach [35]. Lastly, ν and k are computed using the $k - \varepsilon$ turbulent closure model [14].

The temperature and salinity is also affected by external fluxes of surface heat and freshwater. This includes turbulent fluxes of sensible heat Q_{sens} and latent heat Q_{lat}, radiative forcing for thermal (longwave) Q_{LW} and solar (shortwave) Q_{SW} components, and surface evaporation (E) and precipitation (P). These fluxes are imposed as Neumann boundary conditions the the tracer equation.

$$\begin{aligned} K_v \frac{\partial T}{\partial z} &= -\frac{Q_{\text{sens}} + Q_{\text{lat}} + Q_{\text{LW}} + Q_{\text{SW}}}{\rho C_p} - Q_{\text{nudg}}, \\ K_v \frac{\partial S}{\partial z} &= -S(P - E) - Q_{\text{nudg}}, \end{aligned}$$

Where C_p is the water specific heat capacity, and $Q_{nudg} = \Delta z_s \frac{C_0 - C}{\tau}$ is an additional surface relaxation term implemented as a simple data assimilation method for a surface tracer measurement C_0 as a function of a surface mixed layer depth Δz_s, and a relaxation period τ [13]. Surface evaporation $E = -\frac{Q_{lat}}{\rho L_e(T)}$ is a function of the latent heat flux and the latent heat of vaporization $L_e(T)$ defined by Henderson-Sellers [16].

The three-dimensional domain Ω is bounded by static lateral Γ_l and bottom Γ_b boundaries, and includes a dynamic surface boundary Γ_s. Impermeability conditions are imposed on Γ_b and Γ_l, asummed to be strictly vertical.

$$\begin{aligned} w - \mathbf{u} \cdot \nabla_h b = 0 \qquad & \mathbf{x} \in \Gamma_b, \\ \mathbf{u} \cdot \hat{\mathbf{n}}_h = 0 \qquad & \mathbf{x} \in \Gamma_c, \\ w - \frac{\partial \eta}{\partial t} - \mathbf{u} \cdot \nabla_h \eta + s = 0 \qquad & \mathbf{x} \in \Gamma_s, \end{aligned}$$

Where $\hat{\mathbf{n}}_h = (n_x, n_y, 0)$ is the horizontal unit normal vector and $s = (P - E)$ is the water surface source term due to precipitation and evaporation. Full slip conditions are used for the tangential velocity on the closed boundaries (on coastlines) Γ_{lc} and

additional momentum flux boundary conditions are imposed on Γ_b and Γ_s to account for the bottom τ_b and surface τ_s stresses :

$$\nu_v \frac{\partial \mathbf{u}}{\partial z} = \frac{\tau_b}{\rho_0} \qquad \mathbf{x} \in \Gamma_b,$$
$$\nu_v \frac{\partial \mathbf{u}}{\partial z} = \frac{\tau_s}{\rho_0} \qquad \mathbf{x} \in \Gamma_s,$$

Where the bottom stress is imposed with a logarithmic profile :

$$\frac{\tau_b}{\rho_0} = C_d \left|\mathbf{u}_{bf}\right| \mathbf{u}_{bf},$$
$$C_d = \left(\frac{\kappa}{\ln\left(\left(z_{bf} - b\right)/z_0\right)}\right)^2,$$

Where C_d is the bottom drag coefficient, $\kappa \approx 0.41$ is the von Karman constant, z_{bf} the vertical bottom coordinate, $\mathbf{u}_{bf}$ the bottom velocity evaluated at z_{bf} and z_0 is the bottom roughness length. The surface wind stress τ_s is finally defined as :

$$\tau_s = \rho_{air} C_w \left|\mathbf{u}_{10}\right| \mathbf{u}_{10},$$

with ρ_{air} the air density, $\mathbf{u}_{10}$ the wind speed at 10 m above the sea level and C_w the wind drag coefficient computed using the Smith and Banke regression [38].

2.3 Meshing

2.3.1 Slim's mesh structure

To represent the domain, a 3D unstructured mesh is used. It is generated in two steps.

1. 2D horizontal unstructured triangular mesh generation
2. Vertical extrusion of the 2D mesh to obtain a 3D mesh of prismatic elements

The local grid size of the 2D mesh enables to refine the domain near zones of interest. This enables to represent more accurately the complex phenomena that can happen in these locations. The 2D mesh is then extruded vertically to create a 3D mesh.

SLIM offers three options regarding the vertical structure of the mesh (Fig. 14).

- z-layers : These layers are horizontal and flat. This setting transforms the bathymetry into an ensemble of step functions. This configuration is numerically stable but yields a staircase representation of the real physical bathymetry. No smoothing of the bathymetry is required for this method

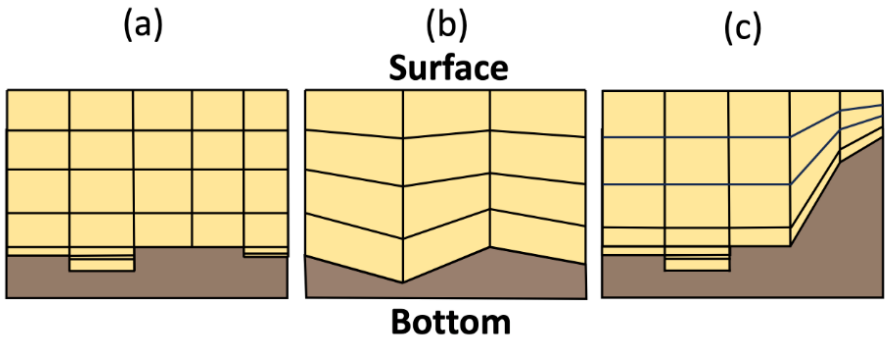


Figure 14: Schematic representation of the vertical discretization strategies available in SLIM3D: (a) z-layer coordinates, (b) terrain-following σ-coordinates, and (c) hybrid σ-z coordinates. [42]

- σ-layers: These layers follow the local bathymetry and are linearly interpolated between grid points. These layers better represent the bathymetry but can yield to numerical errors in areas with sharp bathymetry gradients such as the shelf break. Therefore usually needs to be smoothed in region with steep bathymetry gradients, hence degrading its accuracy.

- Hybrid σ–z layers: This hybrid configuration uses σ-layers in shallow regions to improve accuracy, while employing z-layers in deep regions to enhance model stability at the expense of reduced spatial resolution.

2.3.2 The final mesh

The two dimensional computational mesh was generated using Gmsh [1] and Seamsh [2]. The mesh is locally refined around the reefs on the Queensland Plateau and the GBR. The smallest mesh elements have a characteristic size of approximately 350 m, whereas the largest elements, located outside the region of interest, reach sizes of about 35 km (Fig. 15).

The fine horizontal resolution was selected to accurately capture the local flow variability in the vicinity of the reefs and to remain smaller than the spatial discretization of the reef data itself (500 m; see subsection 2.5). The mesh refinement around the GBR is less pronounced than over the Queensland Plateau, as this region is located farther from the primary area of interest

The two-dimensional mesh was extruded in a three-dimensional mesh using exclusively of vertical z-layers (Fig. 16a). This approach was adopted because the reefs on the Queensland Plateau are located in regions characterized by steep bathymetric gradients. The use of σ-layers would have required a significant bathymetry smoothing

[1] https://gmsh.info/
[2] `https://jlambrechts.git-page.immc.ucl.ac.be/seamsh/index.html`

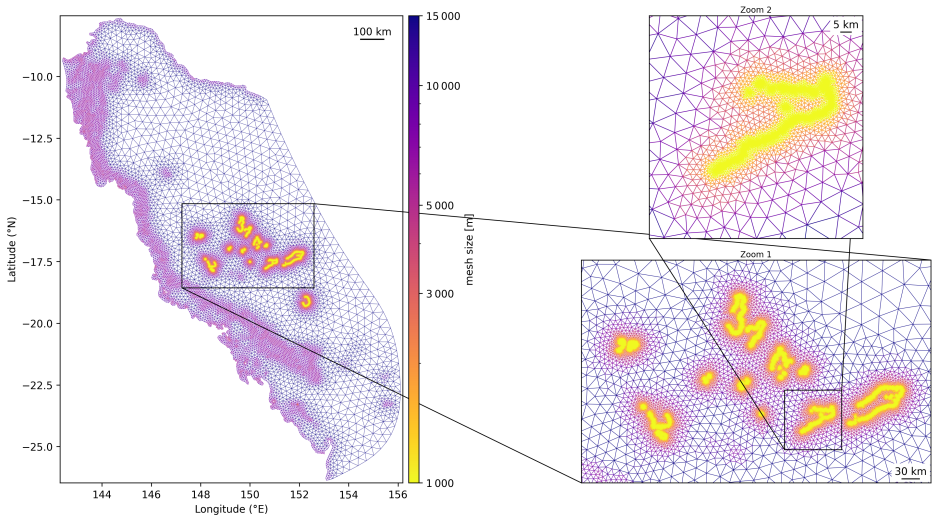


Figure 15: Unstructured two-dimensional computational mesh with local refinement around the Great Barrier Reef and the Queensland Plateau reef systems.

to ensure numerical stability. On the Queensland Plateau, the smoothing would be too important leading to a virtual reduction of the local bathymetry near the studied reefs, reducing the accuracy of the model. To ensure consistency between the simulation bathymetry and the eReefs dataset used for bias calculations (see subsection 2.5), the depth of the z-layers were chosen to match the vertical discretization of the eReefs model. The resulting three-dimensional mesh contains 47 vertical layers, with finer resolution near the surface, where layer thickness can be as small as 1 m, and progressively thicker layers at greater depths.

During the mesh extrusion, the minimum bathymetry is limited to 5.5 m in order to prevent the drying of any region in the domain. This threshold is computed from the maximal value of the tidal cycle during the period combined with a minimum water depth of 3 m. While this approach improves numerical stability, it may affect the accuracy of the results in very shallow reef (< 5.5 m) areas where the actual depth is expected to be lower. Furthermore, because of the staircase discretization of the seabed (Fig. 16b), the simulated bathymetry can present significant differences with the real bathymetry.

2.4 Bathymetry and forcings

The bathymetry used for the mesh generation and the simulation comes from the AusBathyTopo30m2017 dataset. This regional-scale depth model is a compilation of all the available source of bathymetry data in the GBR with a resolution of 30m [3].

For the simulation forcings, two different datasets were employed. Most of the atmospheric forcings were obtained from the high-resolution reanalysis dataset BARRA2, while the surface heat fluxes were derived from ERA5. This choice was motivated by

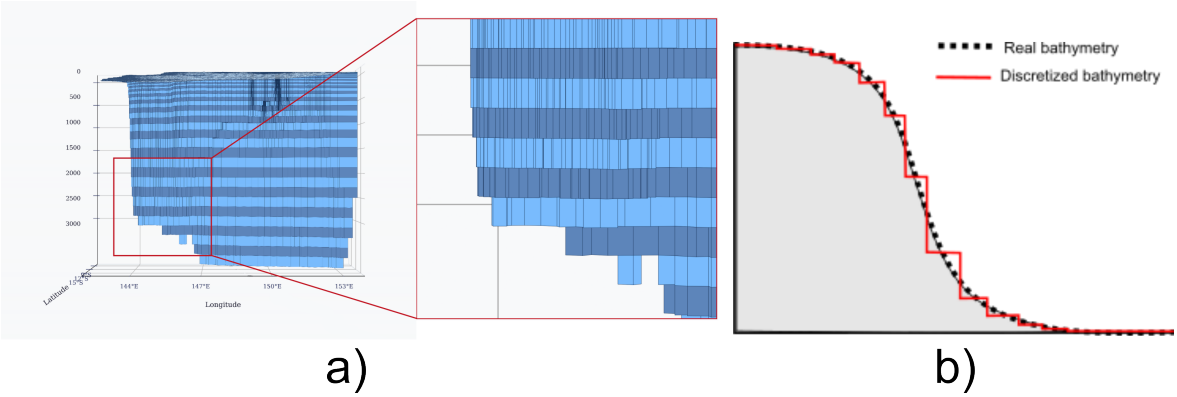


Figure 16: (a) The three-dimensional computational mesh used in the SLIM3D simulations, based on vertically extruded z-layers. and (b) a schematic of the staircase like discretization of the bathymetry using z-layers

the relatively high spatial resolution of BARRA2, approximately 4.4 km [5], which provides a detailed representation of atmospheric conditions over the study area. However, due to an issue identified in the BARRA2 surface heat flux fields, these variables could not be reliably used in the simulations. Consequently, the corresponding surface heat fluxes were taken from the ERA5 dataset instead. The complete list of forcings and their respective data sources is summarized in Table 2.

Forcing	**source**
Wind	BARRA2
Bathymetry	AusBathyTopo30m2017
Tides	BARRA2
Currents	BARRA2
Salinity	BARRA2
Temperature	BARRA2
Air temperature	BARRA2
Surface heat	ERA5
Precipitation	BARRA2
SST	BARRA2
SSS	BARRA2

Table 2: External forcings and datasets used to initialize and force the hydrodynamic simulations. [6], [7], [3]

2.5 Reef depth MMM computation

The computation of cumulative heat stress first requires the estimation of the MMM at reef depth. In this thesis, the method of M. Venegas [43] is followed. The surface MMM climatology is obtained from the NOAA Coral Reef Watch Global 5 km Satellite Sea Surface Temperature Monthly Mean Climatology dataset[3], which provides precom-

[3] `https://coralreefwatch.noaa.gov/satellite/index.php`

puted climatological monthly mean temperatures based on a long-term observational record. From these monthly climatological fields, the MMM is defined as the maximum of the mean monthly temperatures over the annual cycle, and thus represents the warmest typical monthly condition at each spatial location.

To account for the thermal differences between the sea surface and the reef environment, a correction term B is introduced. This bias represents the average temperature difference between the SST and the seabed temperature during the warmest month, defined as the month exhibiting the highest mean SST. The bias is computed as follows :

$$B(\mathbf{x}) = \frac{1}{N_{\text{year}}} \sum_{y=1}^{N_{\text{year}}} \left[\bar{T}_{\text{SST}}(\text{warmest month}, y, \mathbf{x}) - \bar{T}_{\text{seabed}}(\text{warmest month}, y, \mathbf{x}) \right]$$

where $\bar{T}_{\text{SST}}(\text{warmest month}, y, \mathbf{x})$ denotes the average sea surface temperature during the warmest month for year y at position $\mathbf{x}$, and $\bar{T}\text{seabed}(\text{warmest month}, y, \mathbf{x})$ denotes the corresponding average seabed temperature.

In this thesis, the bias term is computed using outputs from the GBR4 v2 model developped by the Commonwealth Scientific and Industrial Research Organisation (CSIRO) [4]. This model has a horizontal resolution of approximately 4 km, 47 vertical layers and provides temperature data from January 2010 to December 2023. The resulting climatology is therefore centered around the year 2017.

However, the NOAA definition of the MMM used in the computation of the DHW metric is based on long-term time series spanning 1985 to 2012, but centered on the 1985–1990 and 1993 periods. The years 1991 and 1992 were excluded from the climatology calculation due to the low accuracy of the data available for those years [32]. This discrepancy in climatological reference periods may introduce a bias in the DHW estimates derived using present methodology. Throughout this thesis, we will assume that the vertical thermal stratification of the water column has remained approximately unchanged since the original NOAA climatological period. While this assumption may be reasonable in deep ocean regions. It is likely to be less accurate in shallow environments, where ocean temperatures respond more rapidly to long-term climate change. The MMM at reef depth is finally obtained by subtracting the bias term from the surface MMM :

$$MMM_{\text{reef depth}}(\mathbf{x}) = MMM_{\text{surface}}(\mathbf{x}) - B(\mathbf{x})$$

[4] `https://thredds.ereefs.aims.gov.au/thredds/resources/docs/gbr4.html`

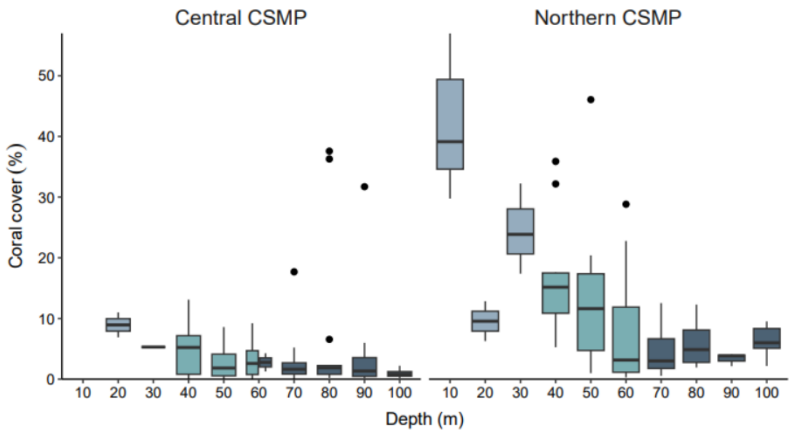


Figure 17: Vertical distribution of coral cover over the central and northern CSMP, illustrating the variability of coral abundance with depth. Adapted from [18].

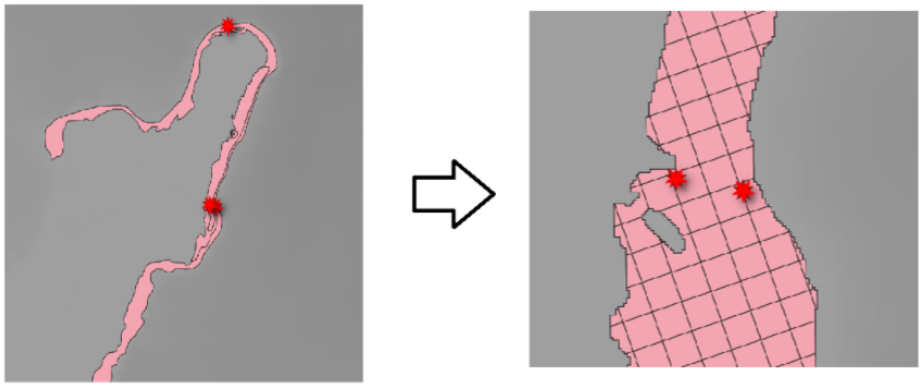


Figure 18: Example of reef discretization using a regular 500 m spatial grid for local thermal stress assessment.

2.6 DHW computation

Several coral reefs exhibit substantial vertical variation in coral cover across depth ranges (Fig. 17, [18]). This vertical heterogeneity highlights the importance of resolving thermal stress over the reef's depth gradient. In addition, local variations in bathymetry and reef morphology may significantly influence exposure to marine heatwaves even within the same reef structure. Therefore, to capture this spatial variability, each reef is discretized into a grid of square cells with a resolution of 500 m (Fig. 18). The MMM at reef depth is then evaluated at the centroid of each grid cell and at the corresponding discretized bathymetry depth. This spatially resolved MMM field is subsequently used to compute DHW over each centroids, providing thermal stress estimates at horizontal resolution of 500 m across all reef systems.

For each centroid, the depth used to compute the bias with the eReefs model is defined as the minimum between the local discretized bathymetry of the hydrodynamic model (SLIM) and the local bathymetry of the eReefs model. Consequently, the bias may be evaluated at mid-water depth in the eReefs model, whereas the same depth

in the SLIM model may correspond to a relatively shallow region. This approach may introduce inconsistencies in the stress metric computation, as the bias does not consistently account for shallow-water processes that may be present in one model but not the other.

$$\text{depth}_{\text{local}}(\mathbf{x}) = \min\left(\text{depth}_{\text{slim}}(\mathbf{x}), \text{depth}_{\text{eReefs}}(\mathbf{x})\right)$$

The bias for this square is then computed using eReefs data at the local depth $\text{depth}_{\text{local}}$. This enables the computation of the reef depth MMM for this square as follows :

$$B(\mathbf{x}) = \frac{1}{N_{\text{year}}} \sum_{y=1}^{N_{\text{year}}} \left[\bar{T}_{\text{SST}}(\text{warmest month}, y, \mathbf{x}) - \bar{T}_{\text{depth}_{\text{local}}}(\text{warmest month}, y, \mathbf{x})\right]$$

$$MMM_{\text{reef depth}}(\mathbf{x}) = MMM_{\text{surface}}(\mathbf{x}) - B(\mathbf{x})$$

The instantaneous heat stress is then computed using SLIM model output as follows :

$$HS\ [^\circ\text{C}] = \begin{cases} 0 & \text{if } T(\text{depth}_{\text{local}}) \leq MMM_{\text{reef depth}} \\ T(\text{depth}_{\text{local}}) - MMM_{\text{reef depth}} & \text{if } T(\text{depth}_{\text{local}}) > MMM_{\text{reef depth}} \end{cases}$$

$$DHW\ [^\circ\text{C} - \text{week}] = \frac{1}{7} \sum_{i=1}^{84} HS_i \text{ when } HS_i \geq 1\,^\circ\text{C}$$

2.7 Validation

In situ observations of hydrodynamic variables over the Queensland Plateau remain sparse. although Acoustic Doppler Current Profiler (ADCP) measurements are available along sections of the GBR coastline, these instruments are located hundreds of kilometres away from the main region of interest and are therefore of limited use for direct validation of the offshore dynamics. Two of them are considered sufficiently close to the region of interest to be used for model validation (Fig. 19).

Additional observational data are provided by the global Argo Program, coordinated by the Intergovernmental Oceanographic Commission and the World Meteorological Organization. This program consists of approximately 4,000 autonomous profiling floats that measure temperature and salinity in the upper 2,000 meters of the ocean. Each float follows a repeating 10-day cycle, during which it descends to a prescribed depth, drifts and then resurfaces to transmit a full vertical profile via satellite

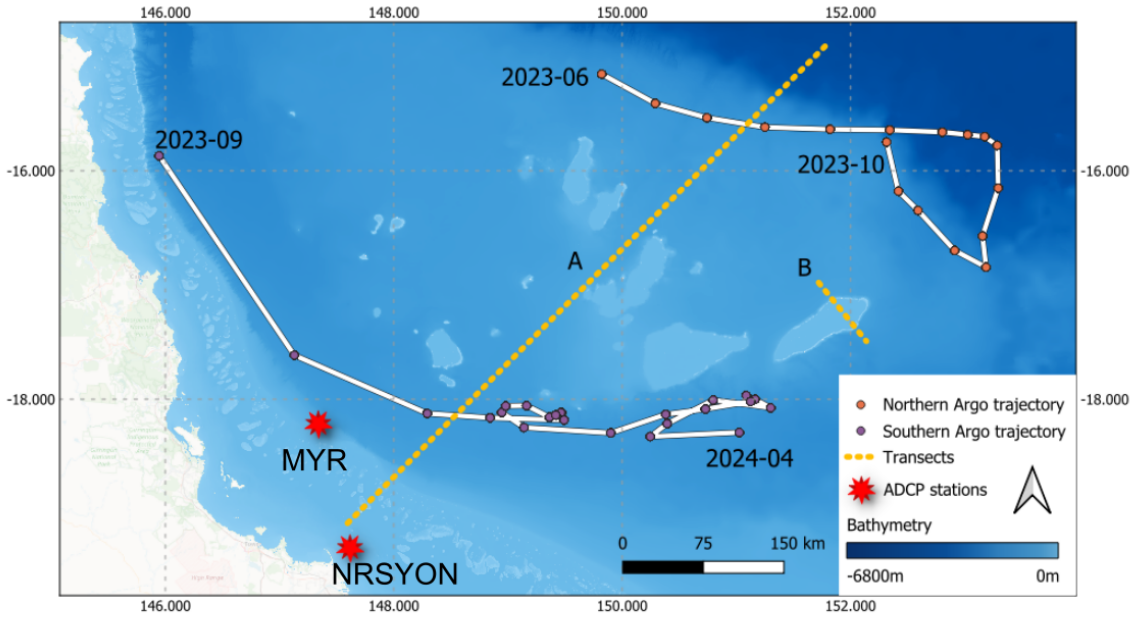


Figure 19: Map showing the trajectories of the two Argo floats and the locations of the two ADCP stations used for model validation. The positions of the two vertical transects used in the analysis are also indicated.

communication [30]. As a result, Argo observations provide quasi-regular time series of vertical temperature and salinity profiles along lagrangian trajectories that evolve with ocean currents.

In this thesis, six Argo floats were identified as passing in the vicinity of the Queensland Plateau during the simulation period. These trajectories are considered suitable for assessing the realism of the simulated hydrographic structure, particularly in offshore regions. All floats pass either north or south of the plateau. For brevity, we will focus only on two floats passing on both sides of the plateau (Fig. 19).

For each Argo profile, the mean relative error will be computed as a function of time for both the vertical temperature and salinity profiles, allowing a quantitative assessment of the model's ability to reproduce the observed hydrographic structure over the trajectory of each float.

Finally, several visualisation tools and diagnostic plots will be used to analyse the simulation outputs and gain insight into the physical processes occurring in the region. In particular, vertical transects across the model domain will be examined. The two transects selected for this study are shown in Fig. 19 and are discussed in section 3.

3 Results

This section presents the results obtained with the model over the period from January 1 to June 1, 2024. The analysis first assesses the model performance through a comparison with available field observations. It then provides an overview of the hydrodynamic conditions over the Queensland Plateau. Finally, the simulated thermal stress patterns across the studied reefs are examined in detail, with a particular focus on two reefs that exhibit strong contrasts between surface and reef-depth thermal stress. The oceanographic conditions at these sites are further analysed to identify the physical processes responsible for the observed differences between surface and depth.

3.1 Hydrodynamic model validation

In order to assess the model validity in vertical dimension, Argo float observations are used. Modelled vertical profiles of temperature and salinity are compared against in-situ measurements, and the mean relative error is computed over the full trajectory of each float.

For the first float passing to the south of the Queensland Plateau (Fig. 19), the vertical structure is better reproduced near the surface than at intermediate depths (Fig. 20a, 20c). The salinity mean relative error (Fig. 20b) increases significantly during the last month of the trajectory, which coincides with the float entering the GBR region, where the model resolution is insufficient to fully resolve the complex dynamics of this area. In the vicinity of the Queensland Plateau, the salinity mean relative error oscillates around 0.25%. The salinity mean relative error over the trajectory is 0.207%, which is considered acceptable. For temperature, the mean relative error (Fig. 20d) fluctuates around 6%, with an average value of 5.79%. This error will be considered as an acceptable range for the present application.

North of the Queensland Plateau, the vertical structure is generally better reproduced. The profiles show only small errors in both SST and SSS (Fig. 21a, 21c). The salinity and temperature mean relative error are lower than in the southern case, with values of 0.188% and 4.031%, respectively (Fig. 21b, 21d). This improved performance can be explained by the relatively simpler bathymetric configuration in the northern Coral Sea, between the Queensland Plateau and Papua New Guinea. In contrast, the southern region between the Queensland Plateau and the GBR is characterized by sharp bathymetric gradients. In addition, the coarser mesh resolution near the GBR likely contributes to reduced model accuracy in this area.

In addition, ADCP stations provide time series of seabed temperature. For the period of interest, the MYR station (Fig. 19) provides measurements that are used to validate bottom temperature in the region. SLIM reproduces the seabed temperature time series at NRSYON with good accuracy, with an Root Mean Square Error (RMSE)

of 0.47 °C and a bias of −0.093 °C. The seasonal cycle is also well captured, with warming during summer and cooling during winter (Fig. 22). A correct representation of the seasonal cycle at seabed depth is essential for the evaluation of thermal stress metrics at reef depth.

The two ADCP station MYR and NRSYON (Fig. 19) are used to evaluate the model performance in reproducing near-GBR currents. At NRSYON, the current speed distribution shows good agreement between SLIM and in-situ ADCP measurements, with an RMSE of $0.143\,\mathrm{m\,s^{-1}}$ and a bias of $0.0047\,\mathrm{m\,s^{-1}}$ (Fig. 23a). However, the directional distribution is less well reproduced. Observations indicate a bimodal current direction, whereas the model predominantly simulates north-westward flow. This discrepancy may result from the coarse mesh resolution near the GBR, which limits the accurate representation of the complex local bathymetry and may affect the simulation of tidal dynamics, particularly in shallow regions where these processes are important.

At the MYR station, slightly higher errors are obtained, with an RMSE of $0.1926\,\mathrm{m\,s^{-1}}$ and a bias of $-0.0494\,\mathrm{m\,s^{-1}}$. The mean current velocity is also lower in the model compared to ADCP observations (Fig. 24a).

Nevertheless, the model reproduces the main current direction more accurately at this location. In particular, a dominant south-eastward flow is well captured, consistent with the recirculation pattern of the SEC. This indicates a satisfactory representation of the main regional circulation pathways.

The spatial structure of the circulation over the full domain further supports these results. Streamline patterns and current magnitudes indicate that the main regional circulation features are well captured by the model. In particular, the East Australian Current (EAC) is clearly visible along the western boundary of the domain. The North Caledonian Jet (NCJ) and the South Equatorial Current (SEC) are also identifiable along the eastern boundary (Fig. 25).

Overall, the model successfully reproduces the large-scale circulation patterns (EAC, SEC, NCJ), realistic vertical stratification, and the correct order of magnitude for temperature and salinity across the domain. Despite local discrepancies near the GBR, the model is considered sufficiently reliable for the analysis of thermal stress at the reef scale.

3.2 Main circulation features

The main circulation patterns over the Queensland Plateau are primarily governed by the South Equatorial Current (SEC), which flows along the northern boundary of the plateau. At the surface level (Fig. 26a), the mean currents are predominantly directed southeastward. In the vicinity of the reefs, the flow is locally deflected due to the presence of shallow bathymetric features and small islets. At deeper levels (Fig. 26b),

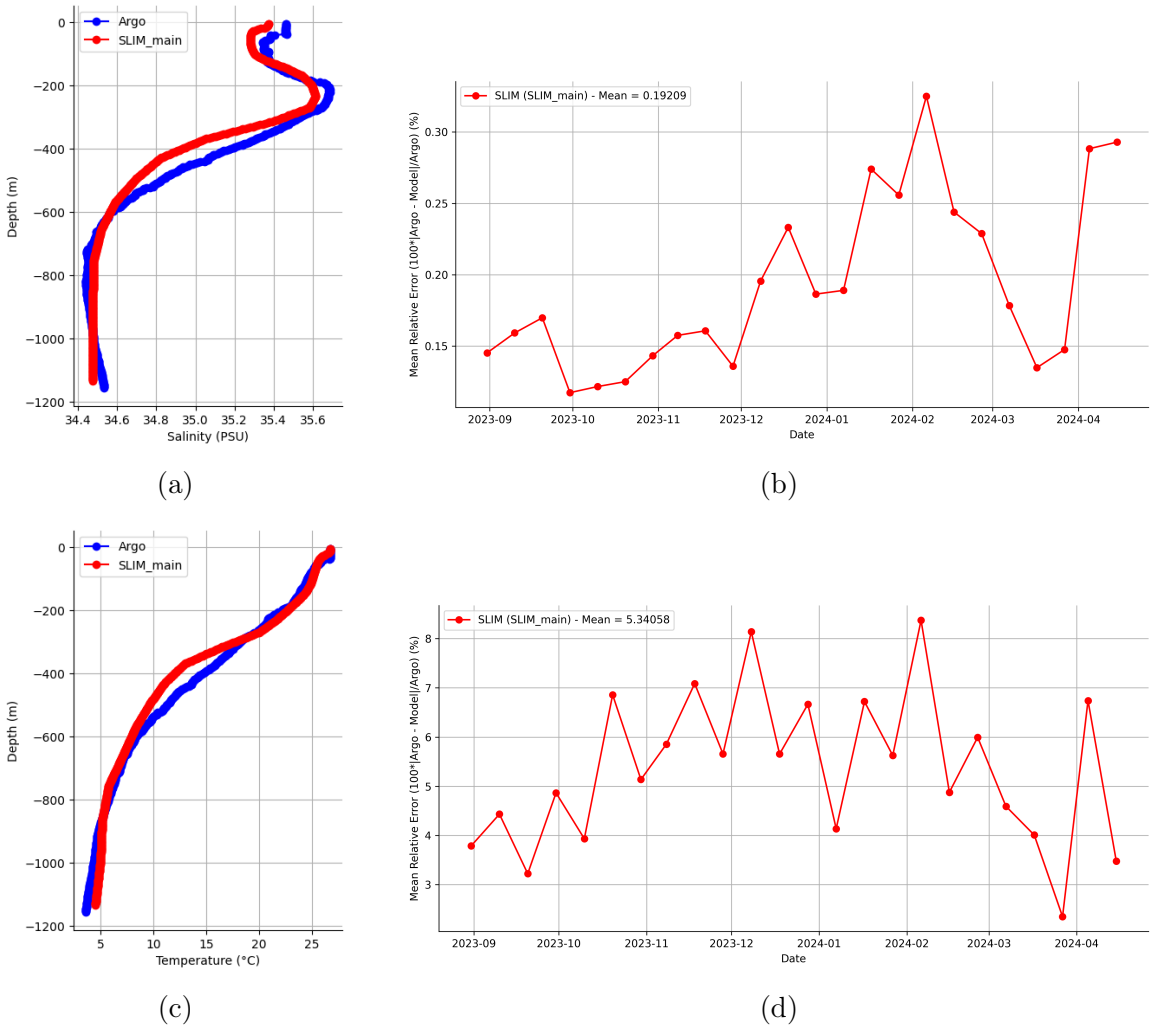


Figure 20: Validation against the southern Argo float, whose trajectory is shown in Fig. 19. Panels (a) and (c) present the vertical salinity and temperature profiles measured by the Argo float and simulated by SLIM on 2023-12-08, respectively. Panels (b) and (d) show the relative mean error over the water column for salinity and temperature, respectively. Overall, low error levels are observed for both variables, demonstrating the model's ability to accurately reproduce the vertical structure of the water column in this region.

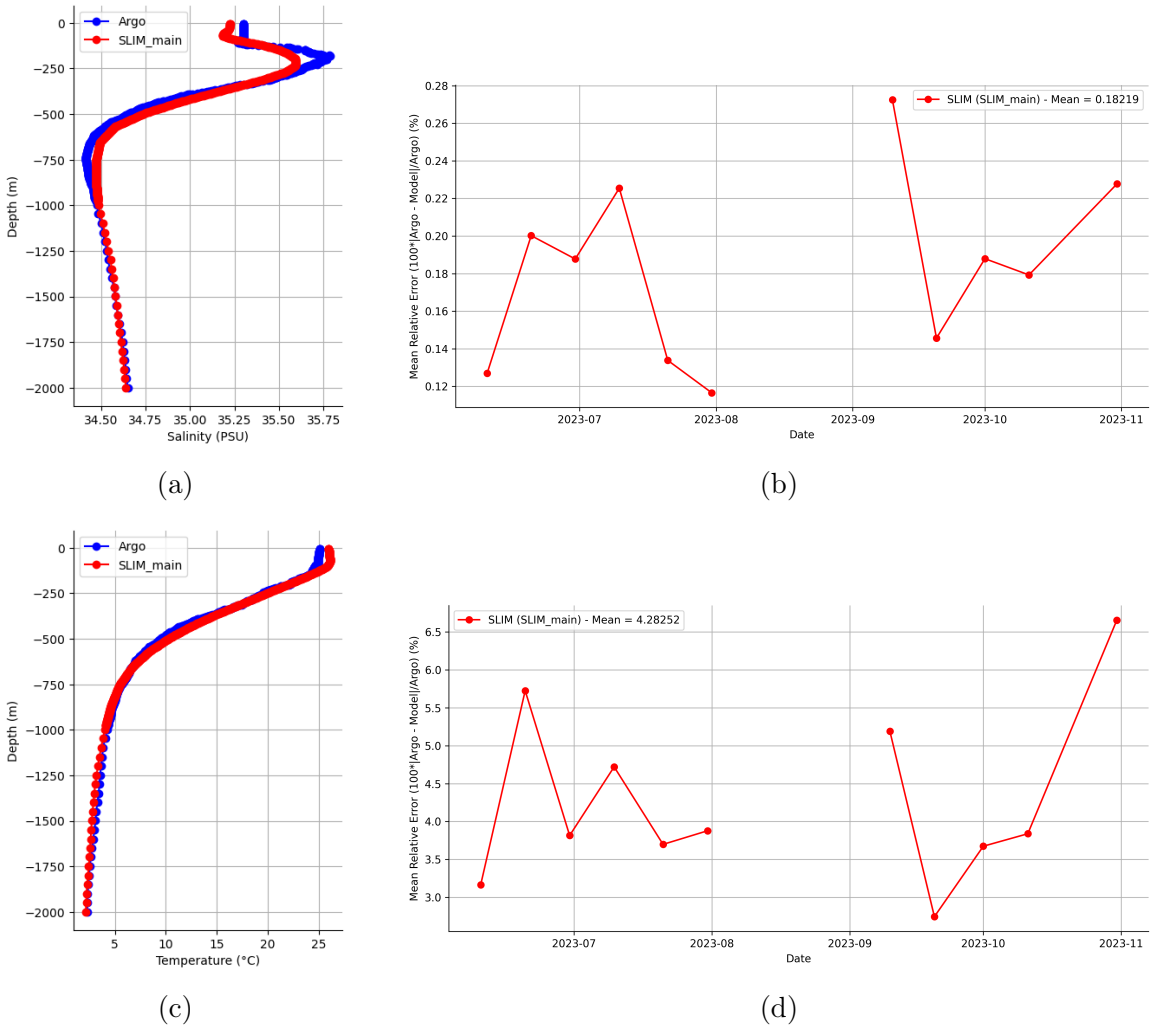


Figure 21: Validation against the northern Argo float, whose trajectory is shown in Fig. 19. Panels (a) and (c) present the vertical salinity and temperature profiles measured by the Argo float and simulated by SLIM on 2023-12-08, respectively. Panels (b) and (d) show the relative mean error over the water column for salinity and temperature, respectively. Overall, low error levels are observed for both variables, demonstrating the model's ability to accurately reproduce the vertical structure of the water column in this region.

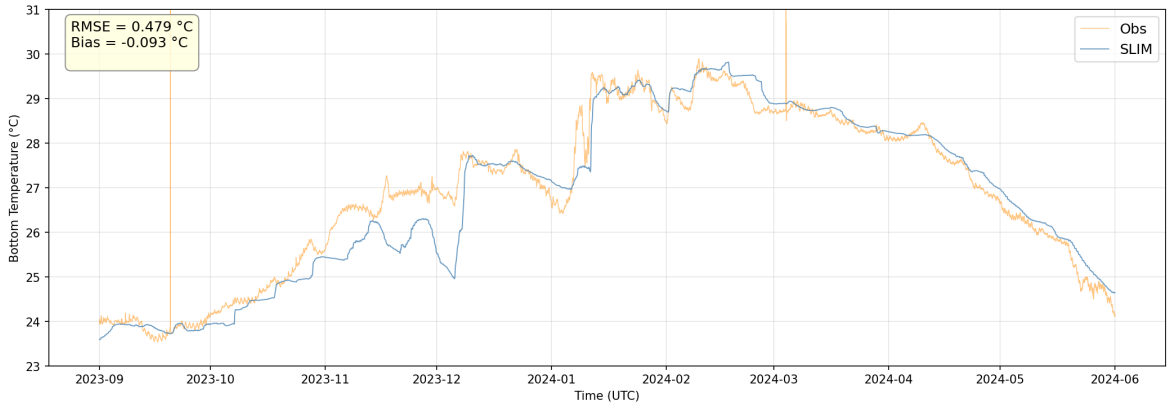
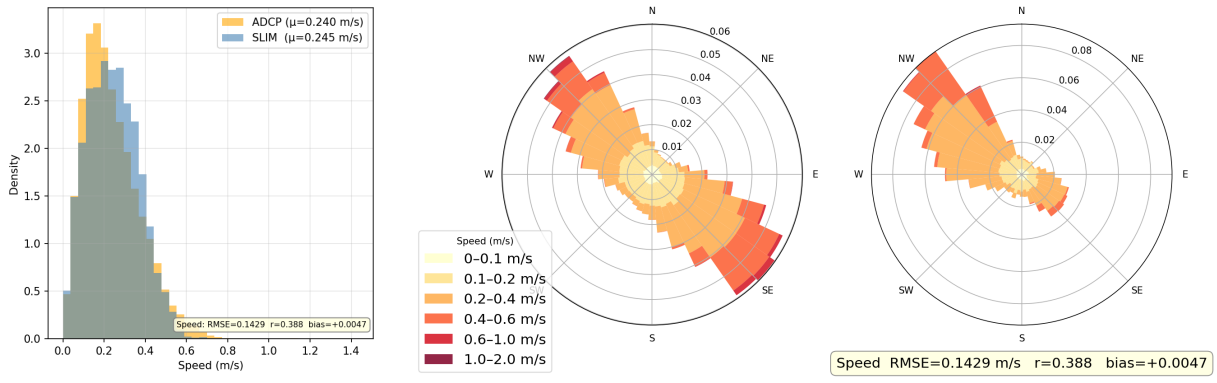
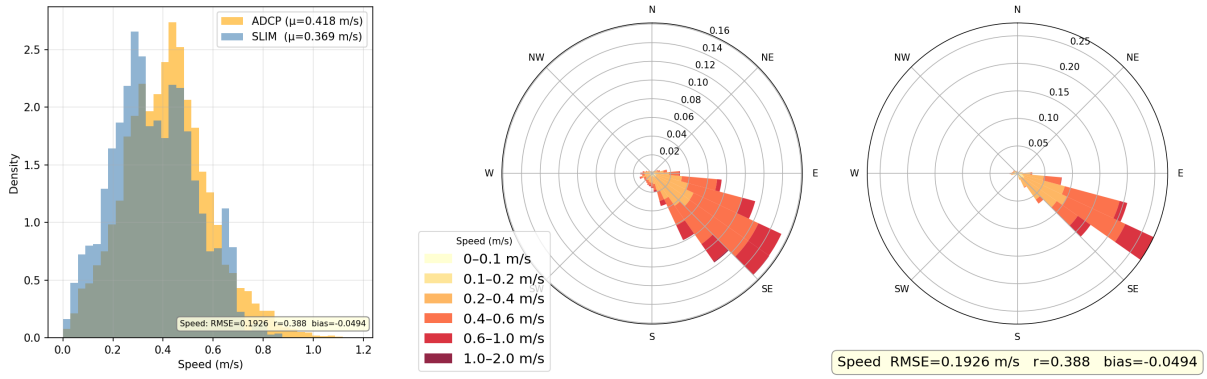


Figure 22: Comparison between modelled and observed seabed temperature time series at the NRSYON station (Fig. 19) over the study period. The model shows good agreement with the *in situ* observations, demonstrating its ability to accurately reproduce the seasonal variability of bottom temperature in this region.



(a) (b)

Figure 23: Comparison between simulated (SLIM) and observed (ADCP) current characteristics at the NRSYON station (Fig. 19) at 8 m depth. (a) Distribution of current velocity magnitude. (b) Directional distribution of currents represented by current roses. These results highlight some inaccuracies in the representation of current direction within the GBR region.



(a) (b)

Figure 24: Comparison between simulated (SLIM) and observed (ADCP) current characteristics at the MYR station (Fig. 19) at 54 m depth. (a) Distribution of current velocity magnitude. (b) Directional distribution of currents represented by current roses. These results show a better representation of the current orientation near the shelf break.

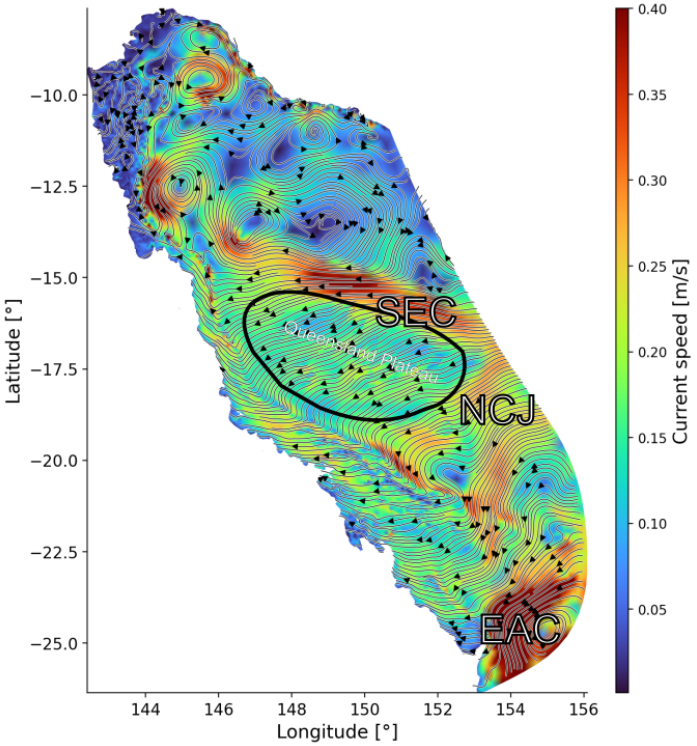
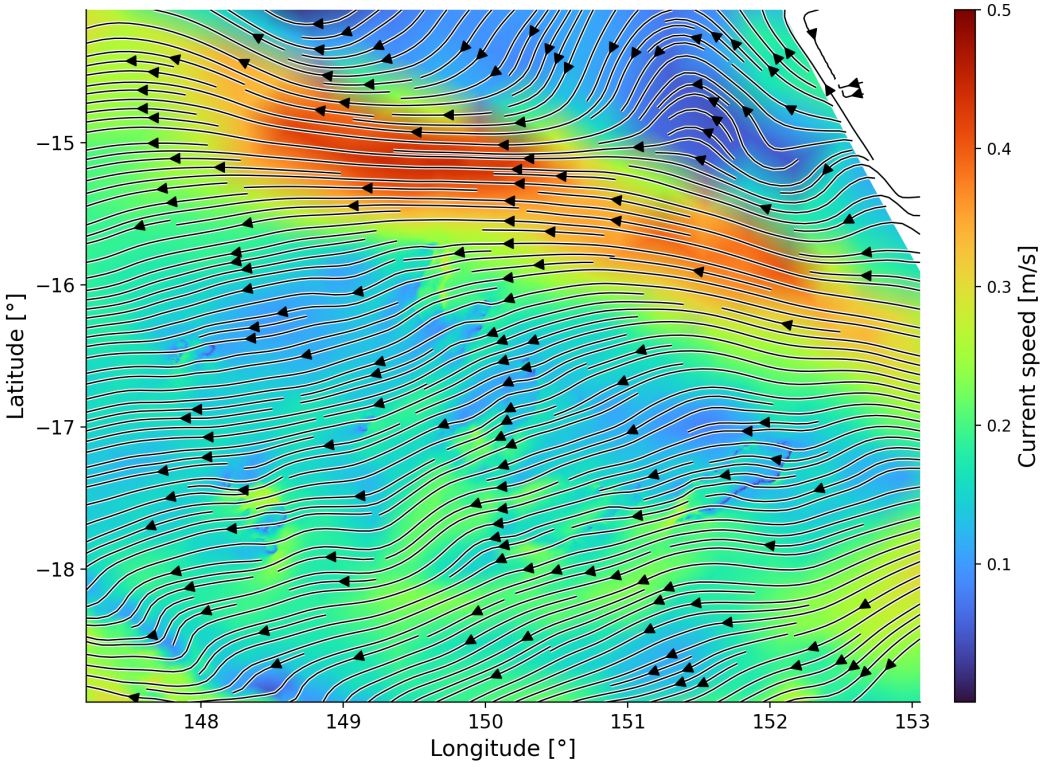
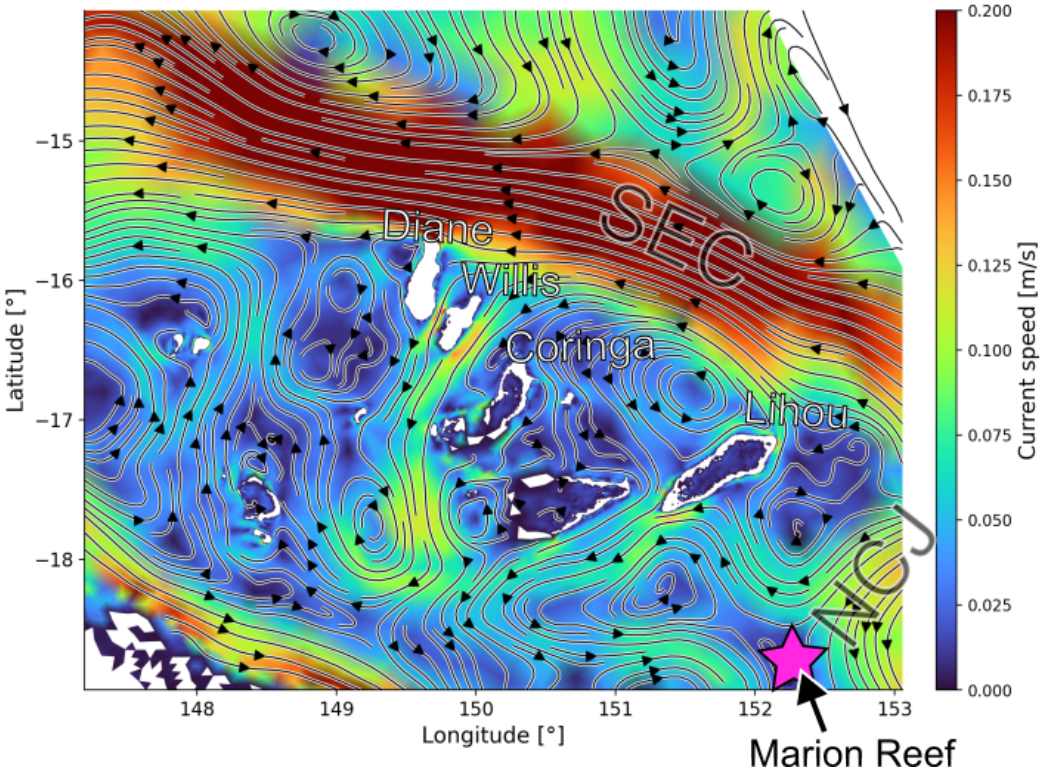


Figure 25: Mean surface horizontal circulation over the period from December 1, 2023, to April 1, 2024. The main features of the circulation are well captured by the model, namely the South Equatorial Current (SEC), the North Caledonian Jet (NCJ), and the East Australian Current (EAC).



(a)



(b)

Figure 26: Mean horizontal circulation over the Queensland Plateau at (a) the surface and (b) 60 m deep during the period from January 1 to May 1, 2024. While the surface circulation is predominantly unidirectional, the flow at depth becomes considerably more complex due to interactions with the reef system, generating localized vorticity and enhanced current velocities in several regions.

the SEC remains the dominant hydrodynamic feature of the region. However, unlike at the surface, the flow between the reefs becomes more complex and no longer exhibits a predominantly unidirectional structure. Numerous eddies and intricate circulation patterns develop, with some areas characterized by intensified currents resulting from the interaction between the flow, the local bathymetry, and the reef structures. These interactions generate localized regions of strong currents. Near Willis Reef, frictional interactions between the Diane Bank and the SEC induce a partial deflection of the current into the reef system. This process generates accelerated currents between Willis Reef and Coringa Bank, as well as between Diane Bank and Willis Reef. Similarly, near Lihou Reef, part of the North Caledonian Jet (NCJ) is diverted toward the reef system due to the presence of Marion Reef, which acts as an obstacle to the flow. This deflection leads to the formation of a large eddy southeast of Lihou Reef and enhances current velocities along the reef slopes as a consequence of the flow reorientation imposed by the local bathymetry.

The vertical structure of the water column across the Queensland Plateau (Fig. 27) shows a stratified structure over the Queensland Plateau. The thermocline is observed around 500 m over the Queensland Plateau but get shallower near the GBR. The current velocity shows a strong fast flowing current pocket between the surface and the depth of -200 m that corresponds to the recirculation of the SEC during the simulated period and the accumulation of the currents flowing across the Queensland Plateau's reef system towards the GBR. In the coral Sea off the Queensland Plateau, strong surface currents are observed corresponding to the SEC.

3.3 Simulated heat stress

This section examines the simulated heat stress metric, Degree Heating Weeks (DHW), over the study period. We begin by analysing the general patterns across the entire Queensland Plateau. Subsequently, two reefs displaying contrasting heat stress responses between surface and depth are investigated in greater detail. For each reef, we explore the physical processes responsible for the observed variations in DHW at reef depth.

3.3.1 Entire Plateau

The simulated surface DHW values are generally lower than those derived from NOAA satellite observations. In the NOAA dataset, most regions of the Coral Sea experienced cumulative thermal stress exceeding 8 DHW during 2024 (see Fig. 28b), whereas the model exhibits extensive areas where thermal stress remains below this threshold (see Fig. 28a). The model successfully reproduces the general spatial tendency of lower DHW values in coastal regions; however, it systematically underestimates the

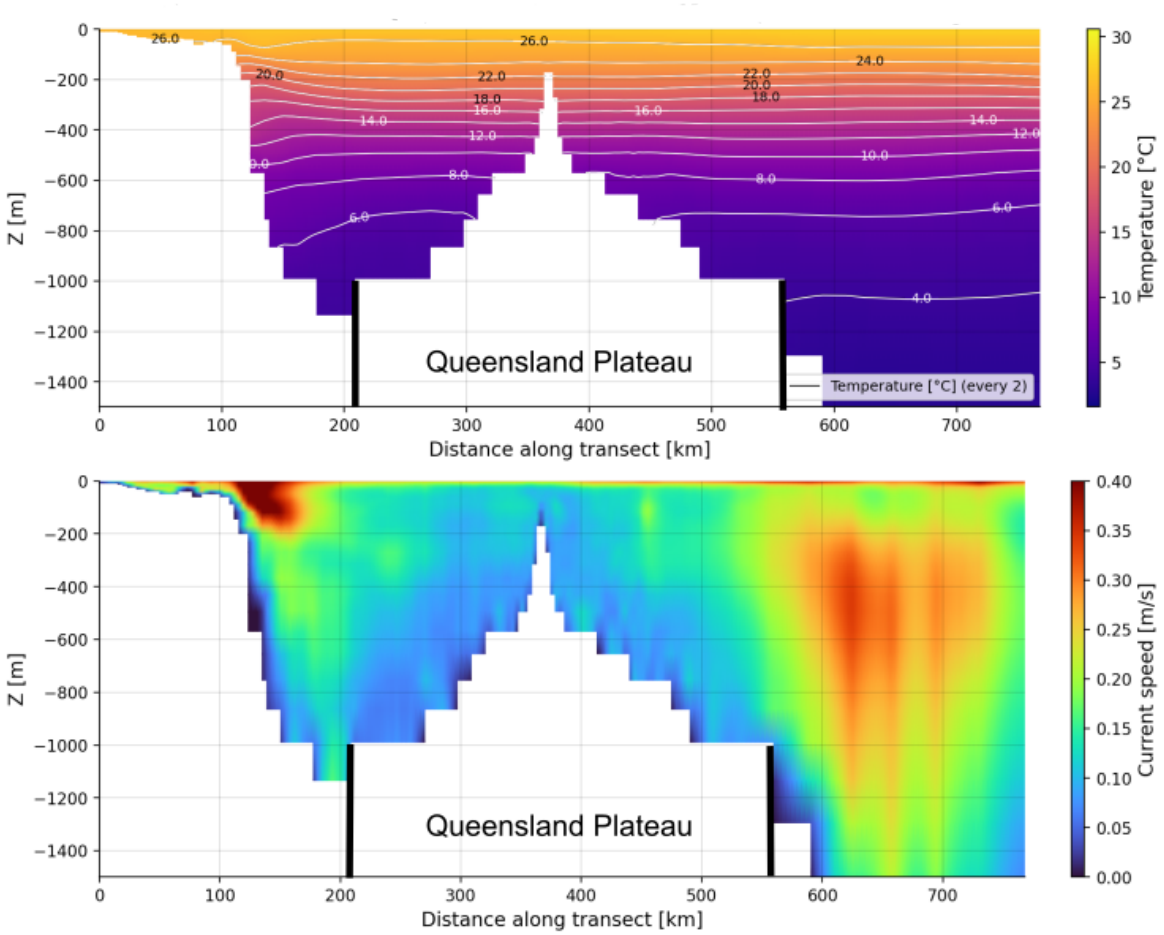


Figure 27: Mean vertical transects of (a) temperature and (b) current velocity during the period from November 2023 to June 2024, along transect A. These plots highlight the strong stratification of the water column in the Coral Sea, as well as the surface currents flowing along both sides of the Queensland Plateau.

absolute magnitude of thermal stress in these areas compared to satellite-derived estimates. Focusing on the Queensland Plateau, the model captures elevated thermal stress levels reaching up to approximately 12 DHW, but fails to reproduce the most extreme hotspots observed in the satellite product, where values can reach 16 DHW. Additionally, the simulation results indicate that the higher spatial resolution in reef-adjacent regions allows the model to explicitly resolve local-scale processes, which are not captured by the coarser 5 km resolution of satellite observations. As a result, important small-scale variability is represented in the model, leading to lower and more spatially heterogeneous maximum DHW values near reefs. In contrast, the coarser satellite product tends to smooth these local features, which can contribute to higher and more spatially aggregated estimates of thermal stress at reef scale.

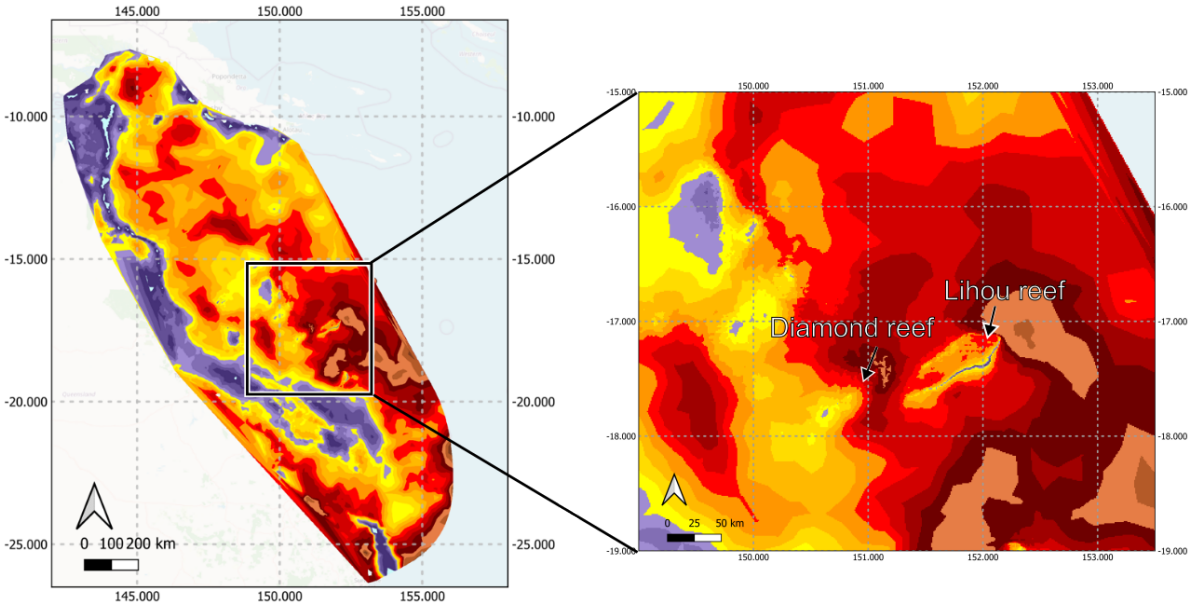
Looking at the differences between maximum DHW values at the surface and at reef depth over the period of interest (Fig. 29), distinct spatial patterns emerge across the Diamond Reef, Holmes Reef, and Coringa Bank. In some regions, thermal stress at reef depth is lower than at the surface, while in others the opposite is observed, highlighting a strong spatial heterogeneity in the vertical structure of thermal stress.

These contrasting behaviours motivate a more detailed investigation of specific reef systems. In particular, the Diamond Reef is selected for further analysis, as some of its locations experienced comparatively lower bleaching levels during the 2023–2024 marine heatwave, while the simulations indicate that thermal stress is locally significantly reduced at reef depth relative to the surface. The Lihou Reef is also examined in detail. Although thermal stress at reef depth is generally higher than at the surface, the reef exhibits a pronounced north–south spatial pattern, with lower surface DHW values observed in the southern region (Fig. 28a).

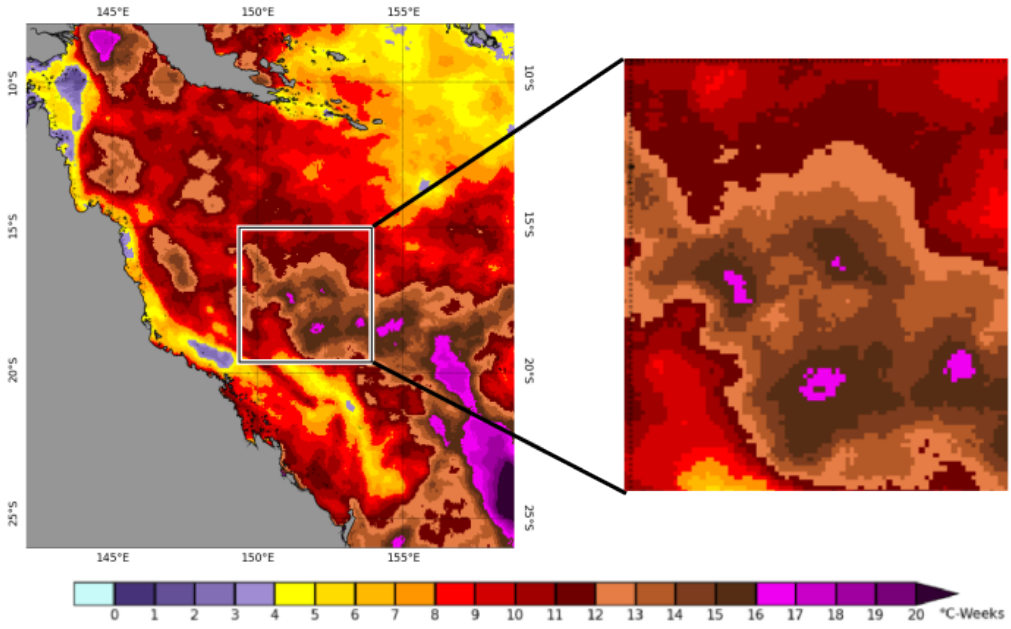
3.3.2 Lihou reef

The southern region of Lihou reef experience smaller heat stress throughout the period of interest. The surface DHW patterns shows a very distinct south-north pattern where to south majorly stays under the 4 DHW whereas the northen region is subjected to 4 to 8 DHW. It can also be noticed that the north-east region shows particularly high levels of DHW over the mortality threshold (8DHW) (Fig. 30a). Looking at the reef depth DHW map (Fig. 30b), we notice higher levels of DHW all over the reef with values over the mortality threshold except in the south part of the reef around 152° where low level of thermal stress (DHW < 4) is observed both in surface and at reef depth. Finally, looking at the difference between the maximum surface and bottom heat stress (Fig. 30c), we observe that the majority of the Lihou reef is experiencing higher DHW values at the reef depth compared to the surface.

Looking at the DHW plots in the south-central region of the Lihou reef (Fig. 31), we observe that the temperature drop between the surface and the reef depth is unper-



(a)



(b)

Figure 28: Comparison between (a) maximum simulated surface DHW and (b) the NOAA Coral Reef Watch 5 km Degree Heating Week Annual Maximum (V3.1) for 2024. Adapted from [31]. This figure highlights that, in general, the simulated thermal stress is lower than the satellite-derived estimates.

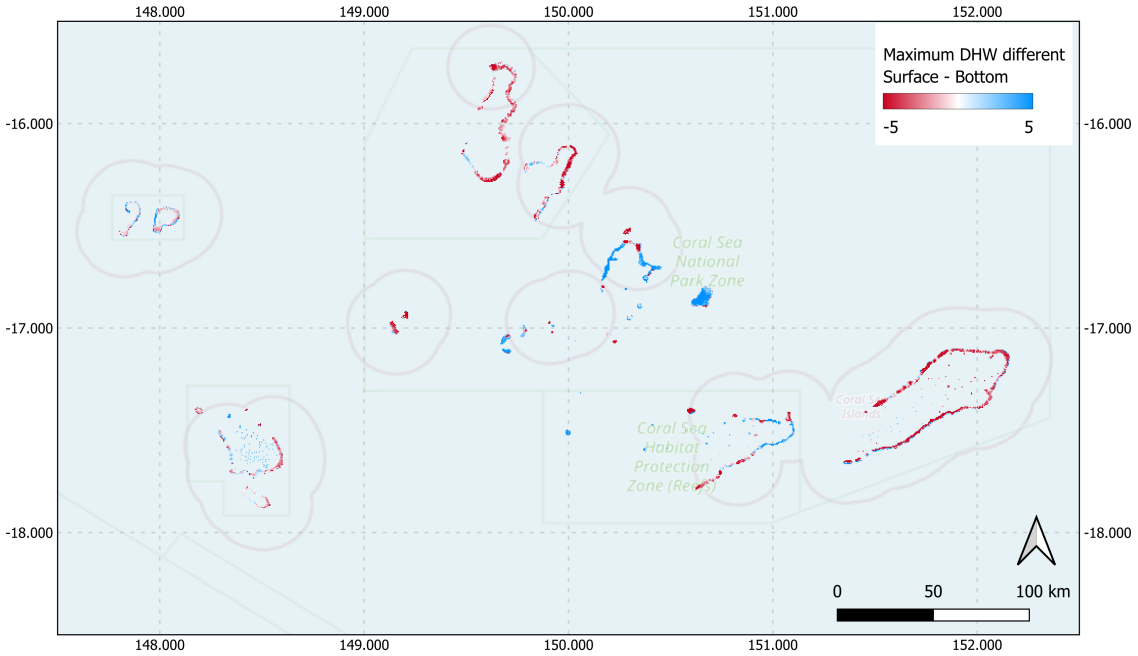


Figure 29: Difference between maximum DHW values at the surface and at reef depth over the Queensland Plateau reefs. This figure highlights that some reefs exhibit locally lower DHW values at depth, whereas others show higher thermal stress at depth than at the surface.

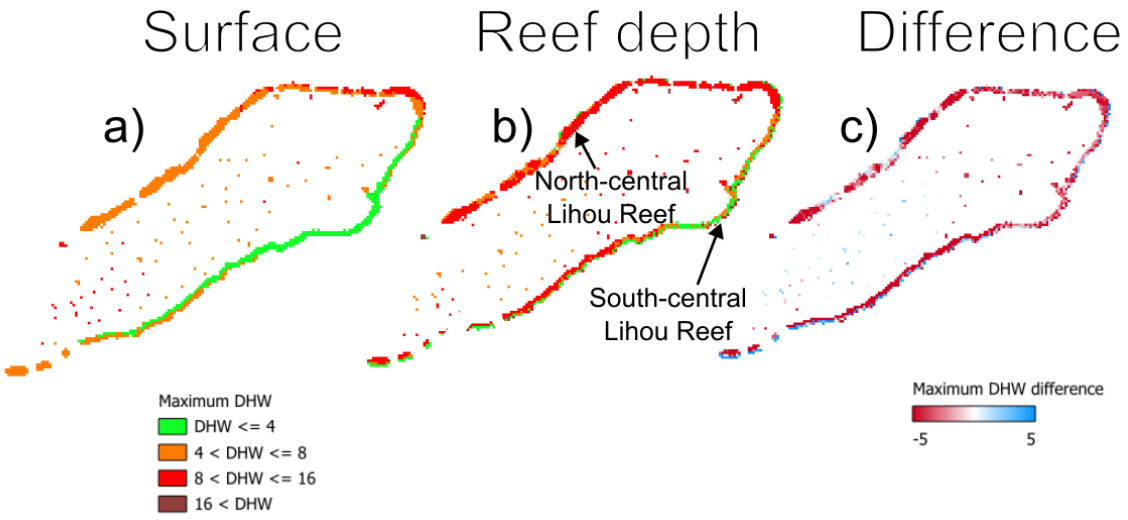


Figure 30: Map of maximum (a) surface DHW, (b) reef-depth DHW, and (c) their difference over Lihou Reef during the period from January 1 to May 1, 2024. The reef is generally experiencing lower thermal stress in the southern region. The reef depth thermal stress is higher than the surface thermal stress over the whole reef.

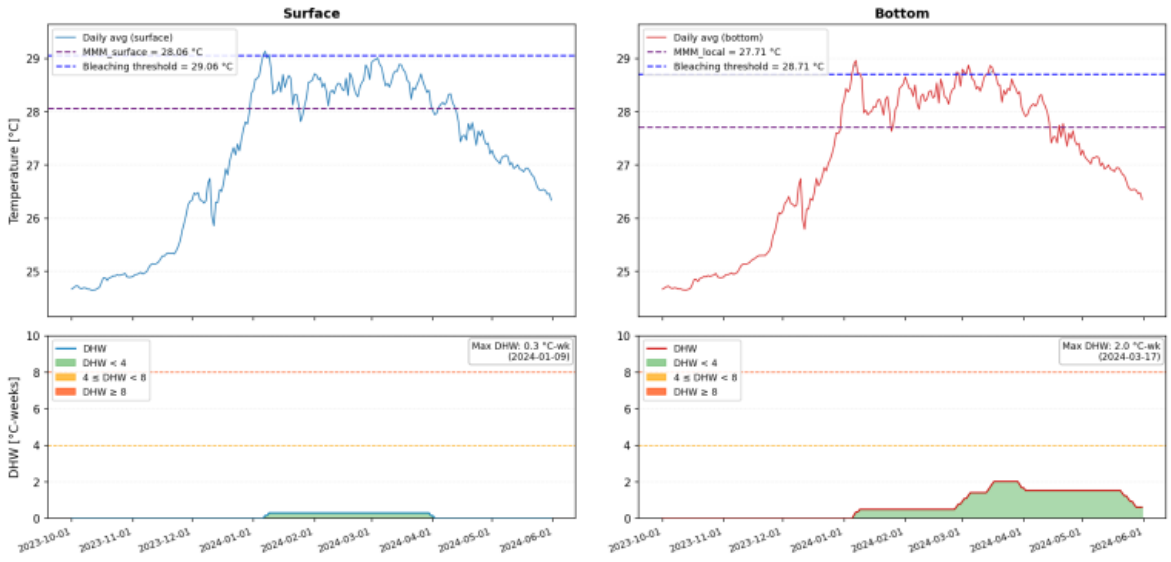


Figure 31: South-central Lihou Reef (depth: 5 m). Temporal evolution of temperature and cumulative thermal stress (DHW) at the surface and at reef depth during the study period. These plots show a very small temperature difference between the surface and reef depth, leading to increased thermal stress at depth due to the lower MMM.

ceptible. As the reef depth MMM is lower than the surface MMM, the daily average temperature exceed the bleaching threshold earlier during the warm season leading to elevated DHW values. Nevertheless, in this region, this phenomenon only causes the reefs to reach DHW levels below 4 DHW in this region.

The north-central region of Lihou reef experiences much higher thermal stress at reef depth than at the surface level. This region present a visible temperature drop between the surface and the reef depth. This temperature drop is not big enough to compensate for the decrease in MMM between the surface and the reef depth. Important levels of DHW are thus observed at reef depth (Fig. 32).

A pronounced north–south contrast in maximum surface temperature can be observed in these plots, with the south-central reef exhibiting peak temperatures during the heatwave approximately 0.5 °C lower than those recorded in the northern part of the reef. At reef depth, temperatures in both regions reach similar maximum values of approximately 29 °C. However, the south-central region is substantially shallower, with a depth of about 6 m, compared to approximately 18 m in the north-central region. Because the MMM decreases with depth, this difference results in higher thermal stress values in the deeper northern region (Fig. 31, Fig. 32).

Looking at the mean SST over the region during the period of interest (Fig. 33a), we observe this north-south difference more clearly. The southern part of the reef experiences lower temperatures than the surrounding region, indicating the presence of phenomena that could protect the corals against marine heatwaves. The lagoon

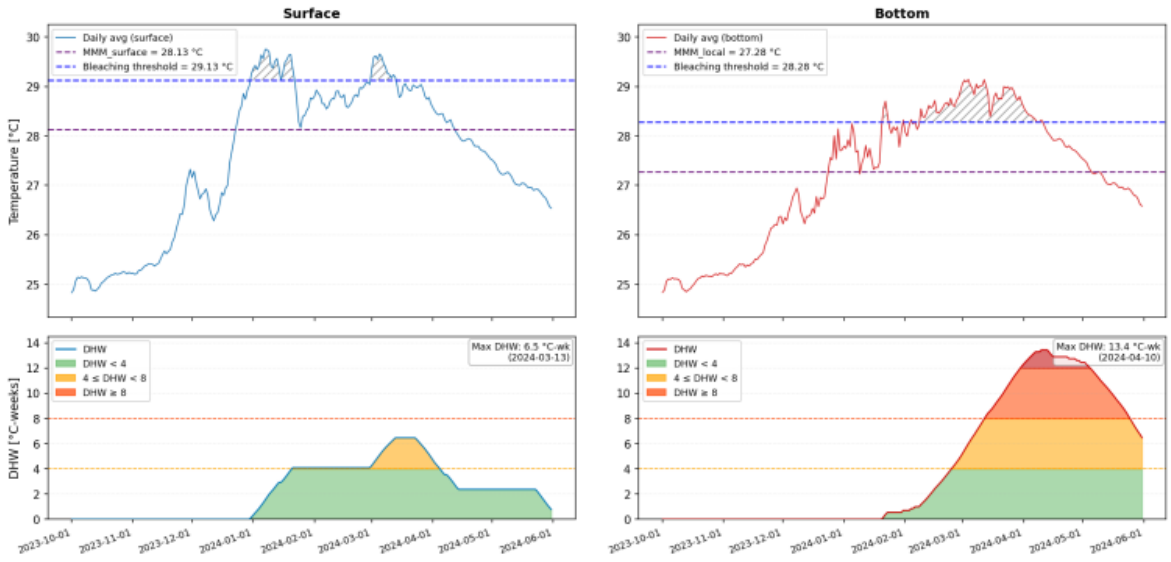


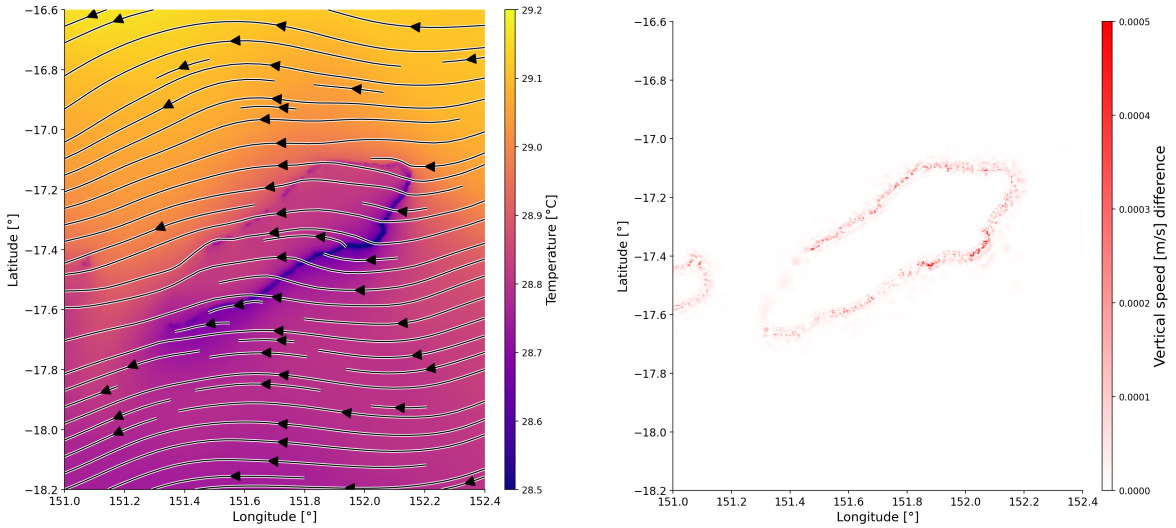
Figure 32: North-central Lihou Reef (depth: 18 m). Temporal evolution of temperature and cumulative thermal stress (DHW) at the surface and at reef depth during the study period. These time series show a clear temperature difference between surface and depth; However, this gradient is not sufficient to reduce thermal stress due to the lower MMM at reef depth, resulting in higher DHW values at depth.

present lower temperatures than the open sea to the North and is explained by the transport of cold water from the south into the lagoon.

Looking at the mean vertical velocity (Fig. 33b), we observe that these colder regions are correlated with areas with positive vertical velocities transporting water from the bottom of the ocean to the surface. Looking at the horizontal circulation at 60 m deep in this region (Fig. 34), we observe again the large eddy created at depth at the south of the reef by the deflection of the NCJ current by the Marion Reef. This eddy generates a relatively important current (0.0075–0.1 $\mathrm{m\,s^{-1}}$) towards the reef slopes. This current is then deflected towards the east and the west along the reef where it gets stronger. At a depth of 20 m and approximately 152.1° longitude, because of the reef topology, the current detaches and the gyre loops on itself.

Looking from farther away, we notice that at the depth of 60 m, this large eddy transport cold water towards the reef and the upwelling zones (Fig. 35a), leading to a reduction of the temperature near the surface in this region. This low temperature region is correlated with a large region of upwelling with a mean vertical velocity around 0.864 $\mathrm{m\,d^{-1}}$ (Fig. 35b). This anti-clockwise eddy is thus pumping cold water from this deep region (1500-2000 m deep).

Finally, looking at the vertical structure of a transect along the low exposure zone, we observe that the isolines are tilted near the southern part of the reef (Fig. 36a), indicating the presence of cold water near the surface explaining the low thermal stress



(a) (b)

Figure 33: (a) Mean Sea Surface Temperature (SST) and (b) vertical velocity over Lihou Reef during the period from 2024-01-01 to 2024-05-01. The SST field shows lower temperatures in the southern part of the reef and within the lagoon compared to surrounding waters, while the vertical velocity field highlights areas of upward motion (positive values) indicative of localized upwelling across the reef system. For clarity, the color scale of vertical velocity is restricted to positive values.

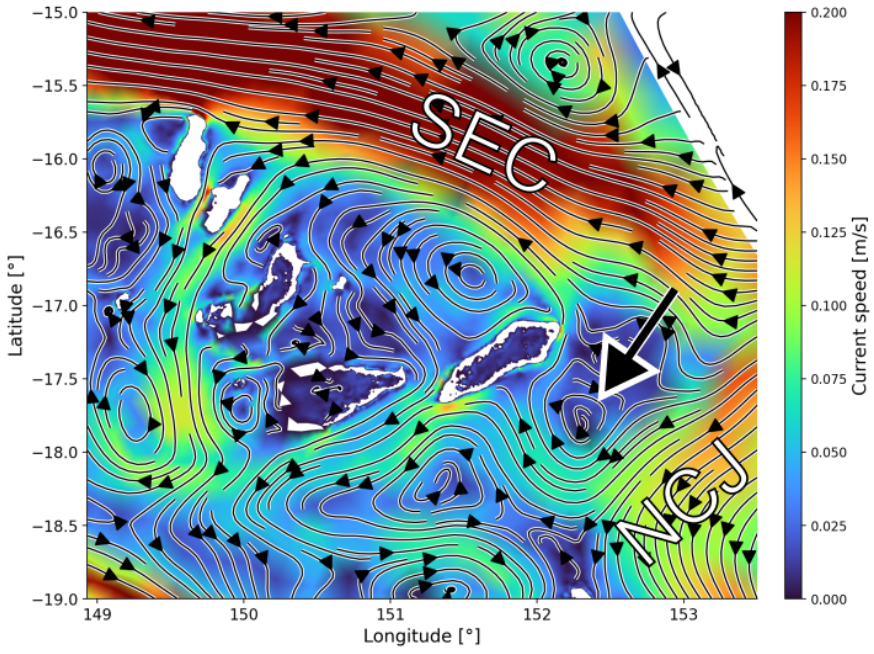


Figure 34: Mean horizontal circulation at 60 m deep around Lihou Reef during the period from January 1 to May 1, 2024. This figure highlights the portion of the NCJ current deflected by Marion Reef and directed toward the southern part of Lihou Reef at relatively high velocity forming a large eddy (indicated by the arrow).

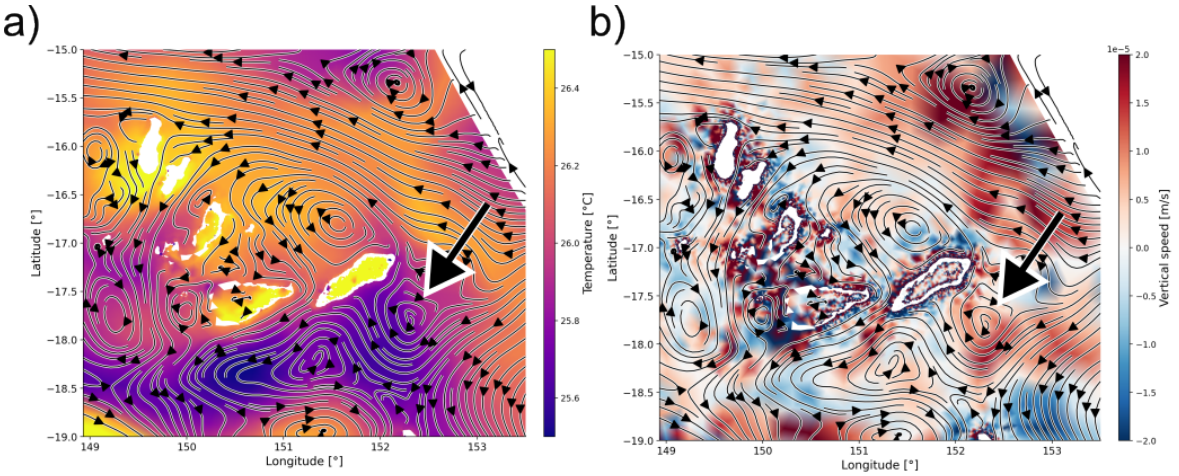


Figure 35: (a) Mean temperature and (b) mean vertical velocity at 60 m depth during the period from January 1 to May 1, 2024. This figure highlights a cold region associated with upwelling induced by eddy pumping linked to the large eddy generated by the NCJ current (indicated by the arrow).

levels. Whereas in the northern part of the reef, the isolines are horizontal, indicating the absence of water colder than the environment in this region. Looking at the mean vertical velocity along the same transect (Fig. 36b), we observe positive vertical velocities on both sides of the reef indicating upwelling in the two regions and emphasizing the role of the large eddy bringing cold water in this upwelling region.

3.3.3 Diamond reef

Diamond Reef exhibits strong spatial variability in thermal stress exposure between surface and reef-depth conditions. Surface DHW distributions reveal two main regions (Fig. 37a). The north-eastern sector experiences severe thermal stress exceeding the coral mortality threshold (DHW > 8), while the south-western sector is characterized by moderate stress levels ($4 <$ DHW < 8). In contrast, reef-depth DHW distributions differ substantially from surface conditions (Fig. 37b). Several locations in the north-eastern sector that experience severe surface thermal stress display significantly reduced stress at depth (DHW < 4). Conversely, portions of the south-western reef exhibit elevated thermal stress at reef depth. Finally, looking at the difference between the maximum thermal stress at the surface and reef depth (Fig. 37c), we observe the whole north-eastern part of the reef experiences lower DHW values at reef depth compared to the surface.

Three locations on the Diamond Reef were identified as refugia and exhibit a consistent reduction of the thermal stress at reef depth (< 4 DHW) whereas the surface DHW exceed 8, the mortality threshold (Fig. 37b). Looking at the DHW timeseries at the southern refugium (Fig. 38), we notice a consistent reduction of both the tem-

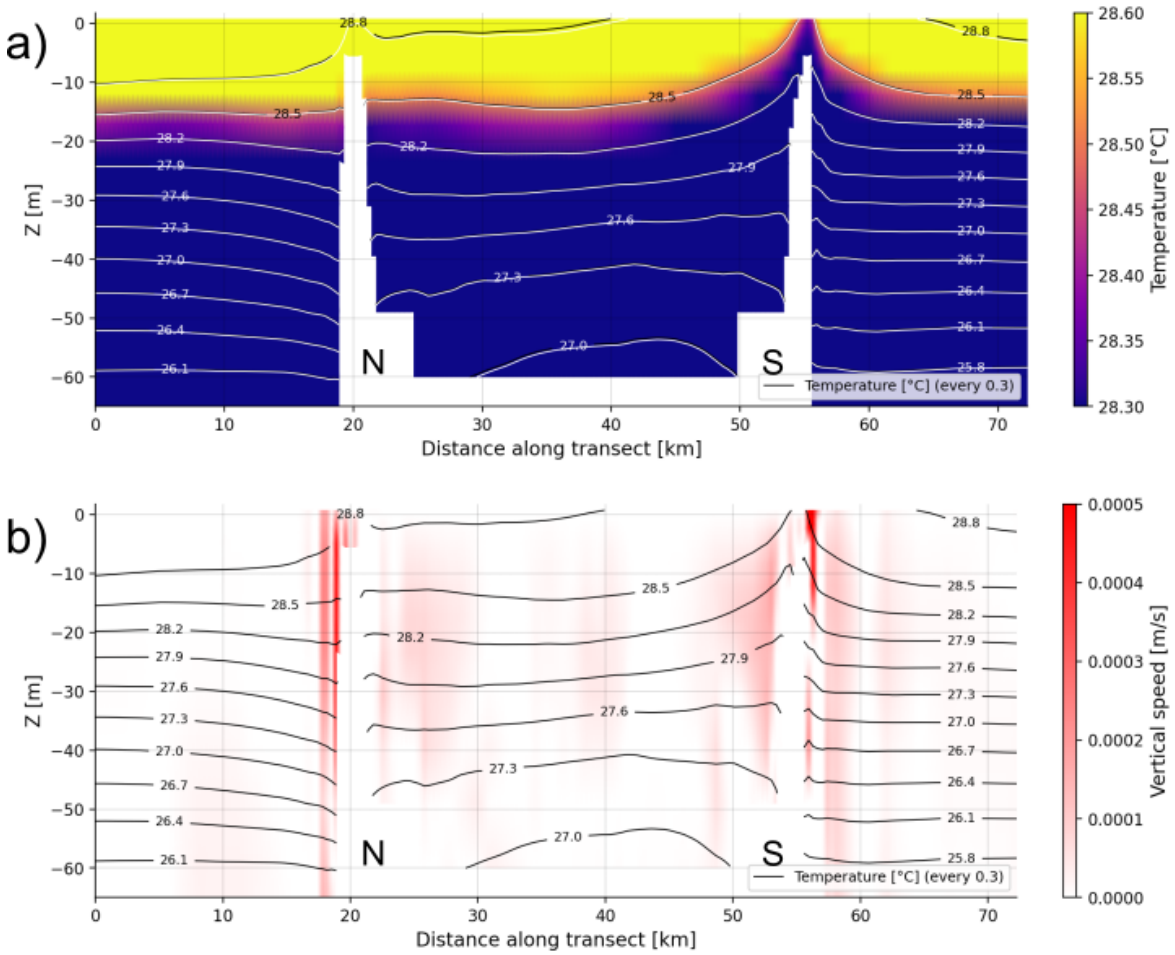


Figure 36: Mean vertical transect of (a) temperature and (b) vertical velocity during the period from January 1 to May 1, 2024 along transect B (Fig. 19). This figure highlights cold-water upwelling along the southern part of the reef. The temperature colorbar is restricted to a narrow range to better emphasize the cold water advected over the southern reef. The southern part of the reef is denoted by S and the northern part by N.

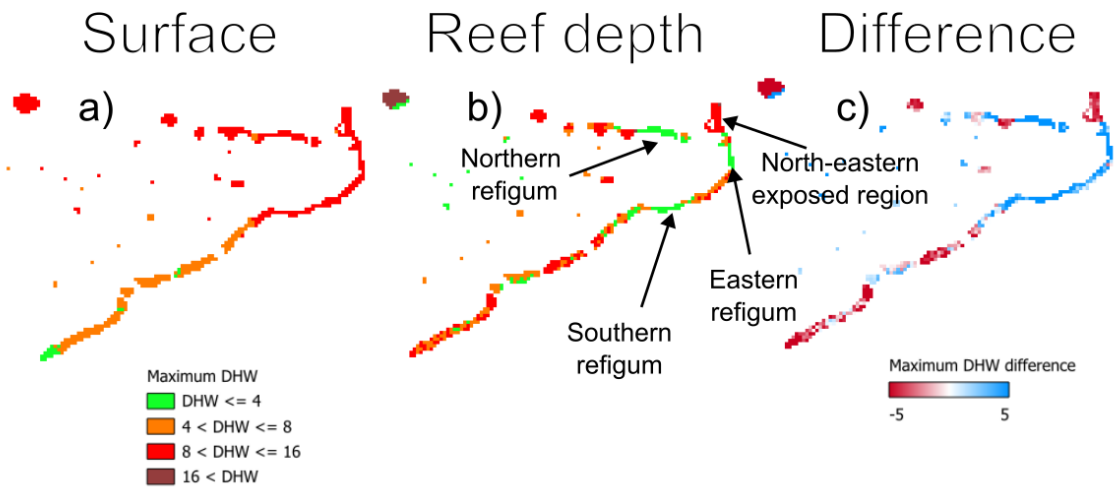


Figure 37: Map of maximum (a) surface DHW, (b) reef-depth DHW, and (c) their difference over Diamond Reef during the period from January 1 to May 1, 2024. The reef exhibits strong spatial variability at depth, with some areas showing high surface thermal stress (>8 DHW) while remaining weakly affected at depth (<4 DHW).

perature and the amplitude of the seasonal warming compared to the surface. While surface warming amplitudes reach approximately 5 °C, reef-depth warming remains limited to approximately 2.5 °C. As a result, temperatures at reef depth exceed the bleaching threshold later in the warm season, typically with a delay of one to two months, and remain above this threshold for shorter durations. These processes significantly reduce DHW accumulation within the refugia (Fig. 38). In contrast, the highly exposed north-eastern region exhibits low temperature differences between the surface and seabed. Because the reef-depth MMM is lower in this area, temperatures exceed the bleaching threshold earlier and persist above it for longer periods, leading to elevated DHW accumulation (Fig. 39).

Hydrodynamic analyses provide further insight into the mechanisms controlling these thermal patterns. The mean horizontal transect at 40 m depth reveals three localized cold-water regions that spatially coincide with the identified thermal refugia (Fig. 40a). These areas are associated with relatively strong horizontal currents reaching approximately $0.1\,\mathrm{m\,s^{-1}}$ (Fig. 40c). The southern refugium additionally exhibits diverging streamlines indicative of vertical motion (Fig. 40c). Vertical velocity fields confirm the presence of upward motion with velocities reaching approximately $0.0014\,\mathrm{m\,s^{-1}}$ ($120\,\mathrm{m\,d^{-1}}$) (Fig. 40b). The northern and eastern refugia display similar but weaker vertical velocities, with magnitudes around $70\,\mathrm{m\,d^{-1}}$. These observations suggest that vertical exchanges contribute to the maintenance of cooler reef-depth conditions.

Time-series analyses further demonstrate the recurrent intrusion of cold water near the seabed within the refugia (Fig. 41a). These intrusions are systematically associated with currents flowing into the Diamond Lagoon (Fig. 41b), indicating advective trans-

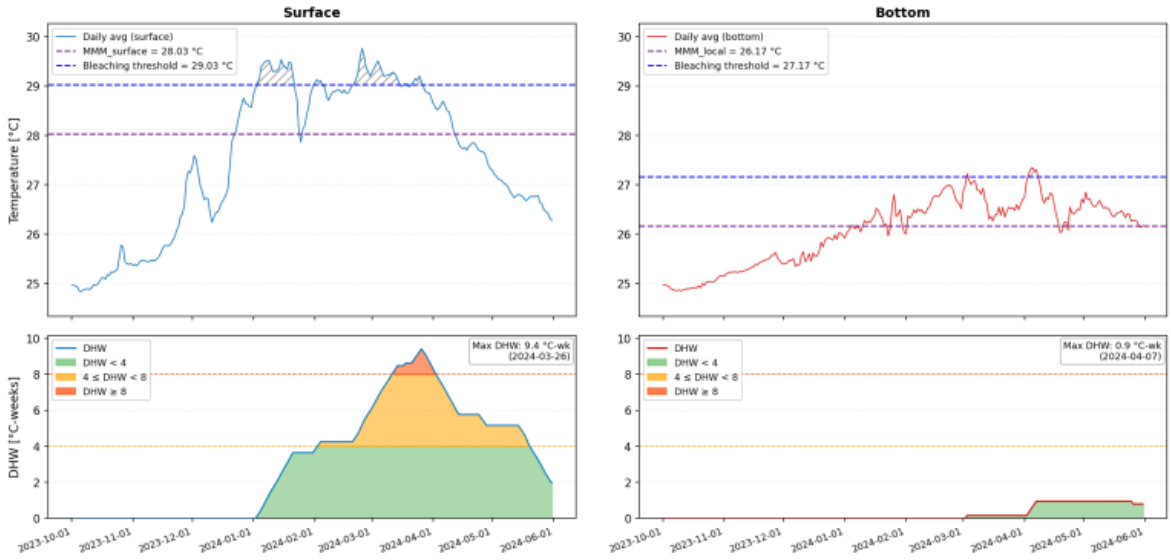


Figure 38: South-central Diamond Reef (depth: 40 m). Temporal evolution of temperature and cumulative thermal stress (DHW) at the surface and at reef depth during the study period. These time series show reduced temperature variability and lower warming amplitude at depth compared to the surface, resulting in delayed exceedance of the bleaching threshold and reduced DHW accumulation.

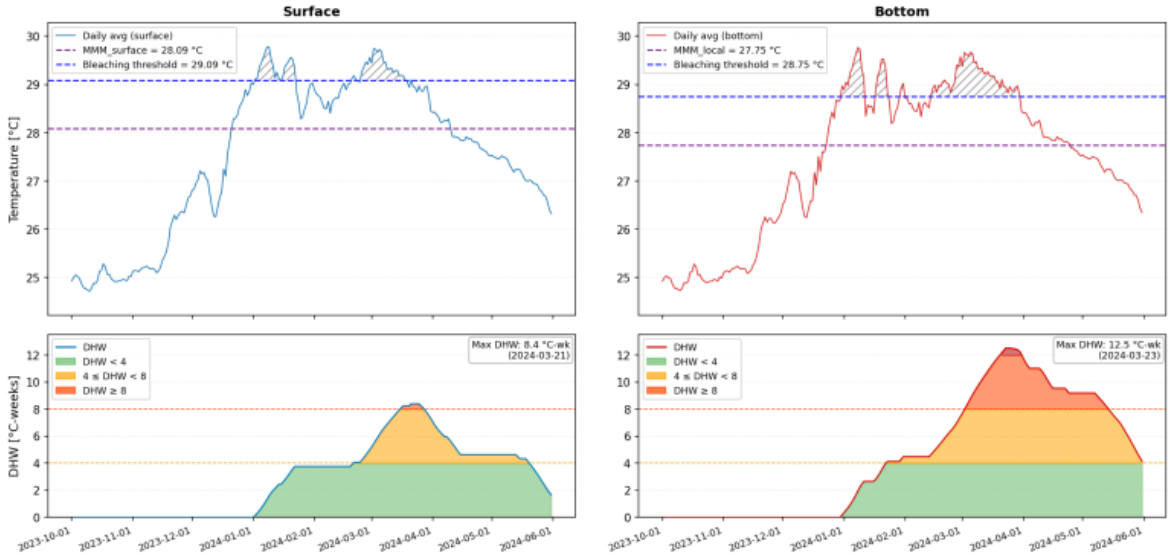


Figure 39: North-eastern exposed region of Diamond Reef (depth: 5.5 m). Temporal evolution of temperature and cumulative thermal stress (DHW) at the surface and at reef depth during the study period. These time series show weak vertical temperature differences, leading to early and prolonged exceedance of the bleaching threshold at depth and high DHW accumulation.

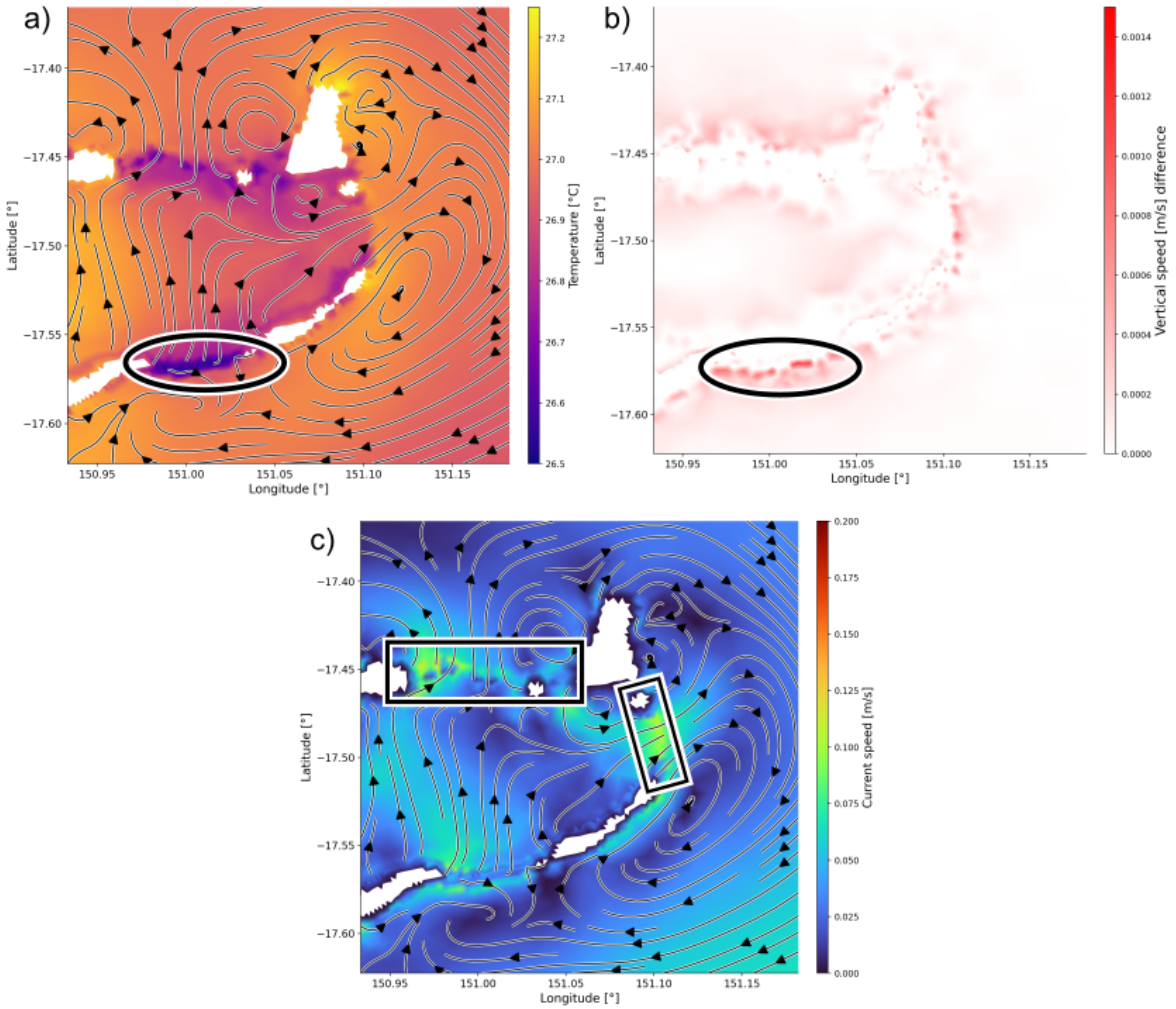


Figure 40: Mean (a) temperature, (b) vertical velocity, and (c) horizontal current velocity at 40 m depth near Diamond Reef during the period from January 1 to May 1, 2024. Ovals indicate regions of divergent streamlines and positive vertical velocities, while rectangles highlight areas of fast-flowing currents. For clarity, the colormap of vertical velocity is restricted to positive values.

port of cooler offshore waters toward the reef. Spectral analyses (details in Appendix B) reveal a clear vertical differentiation in temperature variability. Near the seabed, temperature oscillations are dominated by high-frequency variability with periods close to 12 h, corresponding to the principal semi-diurnal tidal mode. In contrast, the upper water column is characterized by much lower-frequency variability. The power spectral density of seabed temperature further confirms the tidal influence on bottom thermal variability. The northern and eastern refugia exhibit similar hydrodynamic and thermal behaviour. Both regions experience recurrent intrusions of cold water associated with currents entering the lagoon. In both cases, the lower water column is dominated by tidal-frequency temperature oscillations (12 h–24 h), whereas the surface layer exhibits low-frequency variability. Similarly, spectral analyses reveal the same two dominant peaks associated with tidal and atmospheric forcing. The timeseries for these two refugia can be found in Appendix A

In contrast, the highly exposed north-eastern sector displays markedly different dynamics. The shallow water column remains weakly stratified throughout the study period (Fig. 42a), and seabed temperature variability is strongly reduced, with amplitudes limited to approximately 0.6 °C. This contrasts sharply with the refugia, where bottom temperature oscillations can reach 2 °C. Although tidal current reversals with 12 h periodicity are still observed (Fig. 42b), these currents are not clearly associated with cooling events. Temperature variability throughout the water column is instead dominated by slow fluctuations, indicating gradual thermal evolution rather than tidally driven cooling.

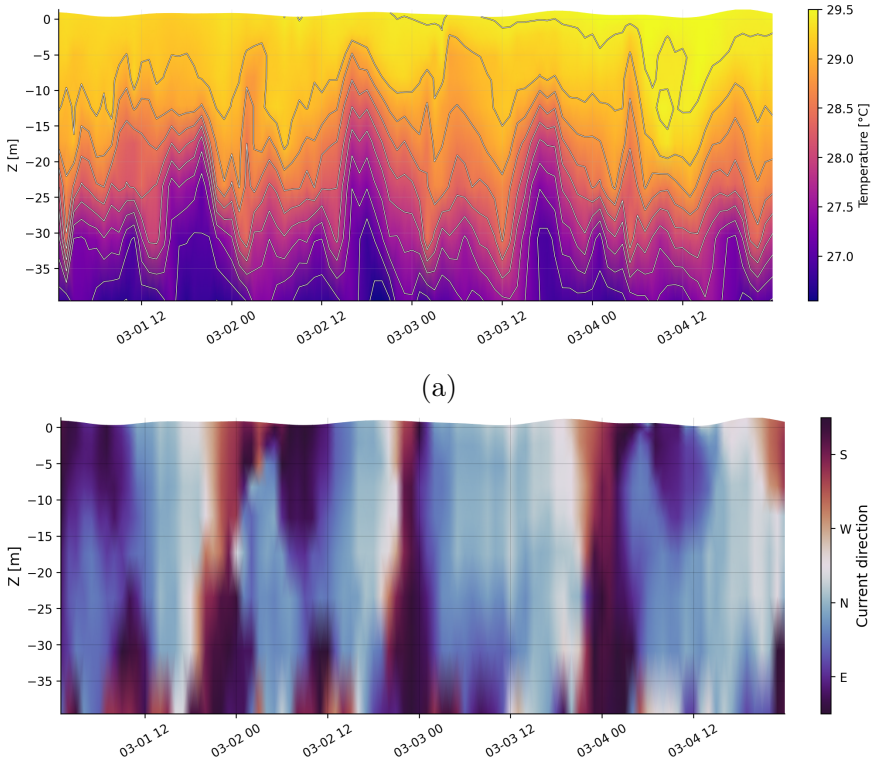


Figure 41: Vertical profile time series of (a) temperature and (b) current direction at the southern refugium (Fig. 37) during the period from January 1 to May 1, 2024. These figures highlight the intrusion of cold water into the Diamond lagoon following a 12-hour cycle linked to the tidal regime in this area.

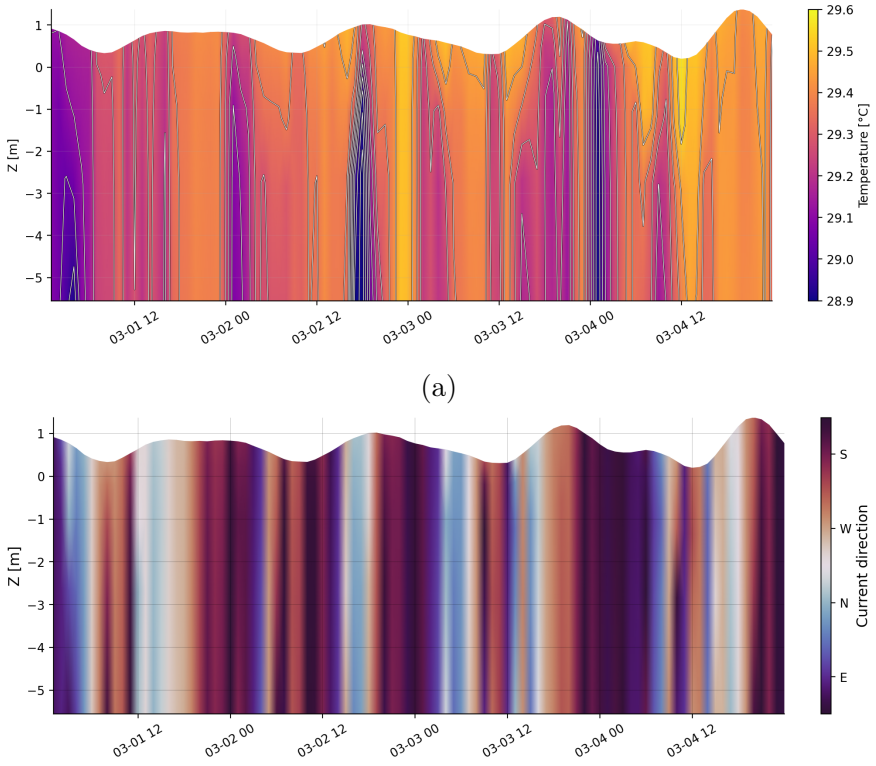


Figure 42: Vertical profile time series of (a) temperature and (b) current direction at the north-eastern exposed region (Fig. 37) during the period from January 1 to May 1, 2024. These figures highlight weak vertical temperature differences in this region and the absence of cold-water intrusion driven by tides.

4 Discussion

4.1 Lihou and Diamond reefs exposure to marine heatwaves

The results of this study highlight that two distinct mechanisms can create favourable thermal conditions for coral survival at Lihou and Diamond reefs, emphasizing the multiscale nature of reef refugia.

At Lihou Reef, the reduced thermal stress observed in the southern region appears to be primarily driven by large-scale ocean circulation processes. The deflection of the North Caledonian Jet by surrounding reef structures promotes the formation of a mesoscale eddy, which in turn induces persistent upwelling of cooler subsurface waters toward the reef. This upwelling mechanism, previously identified in the Capricorn region by Weeks [44], therefore represents a key driver of regional cooling. It suggests that the thermal protection observed at Lihou is governed more by regional ocean dynamics than by strictly local processes. Consequently, the resilience of this reef may be sensitive to changes in large-scale circulation patterns, particularly under climate-driven modifications of western boundary currents. More broadly, these results show that mesoscale circulation can generate persistent thermal refugia capable of locally mitigating the impacts of marine heatwaves. This challenges the assumption that reef-scale processes solely dominate coral thermal exposure and highlights the importance of basin-scale ocean variability.

In contrast, Diamond Reef exhibits a fundamentally different behaviour, where thermal mitigation is primarily controlled by local-scale hydrodynamic processes. The reef's complex topography, characterized by multiple notches, enhances tidal current acceleration and promotes recurrent intrusions of cooler water from the depth into the lagoon. These tidally driven exchanges generate strong high-frequency thermal variability at reef depth, effectively limiting the accumulation of heat stress. Unlike Lihou Reef, this mechanism does not depend on regional circulation patterns but instead arises from the interaction between tidal forcing and fine-scale bathymetry. As a result, Diamond Reef refugia may be more resilient to large-scale circulation changes, yet more sensitive to local morphological characteristics and variations in tidal amplitude. Similar processes have been previously described by Thompson and Golding [41] in the Great Barrier Reef, and our results extend these findings by showing that tidal exchanges not only produce transient cooling events but also significantly reduce cumulative thermal stress (DHW), thereby reinforcing their importance for long-term coral resilience.

Overall, these results highlight that coral reef thermal refugia on the Queensland Plateau cannot be attributed to a single dominant process, but instead emerge from the interaction between regional ocean circulation and local-scale bathymetry. This distinction is critical for future projections, as these mechanisms are likely to respond

differently to climate change. Taken together, the findings demonstrate that reef-scale thermal refugia are shaped by distinct physical drivers operating across multiple spatial scales: Lihou Reef is primarily influenced by mesoscale circulation and upwelling associated with regional dynamics, whereas Diamond Reef is governed by fine-scale tidal processes and local bathymetric features. This contrast underscores the need for a multi-scale framework to predict coral refugia, integrating both large-scale oceanographic variability and local reef hydrodynamics.

4.2 Limitations and perspectives

Despite the overall good performance of the model, several limitations should be highlighted. First, the spatial resolution of the mesh remains relatively coarse in the vicinity of the Great Barrier Reef (GBR). This may reduce the accuracy of the simulated circulation between the GBR and the Queensland Plateau, where important recirculation processes associated with the South Equatorial Current (SEC) occur. In addition, the use of a staircase representation of the bathymetry can introduce discrepancies in the simulation. In particular, this approximation may affect the representation of vertical processes such as upwelling in regions where bathymetric gradients are not adequately resolved.

Another major limitation is the presence of a surface temperature bias in the model, which leads to an overall underestimation of DHW compared to NOAA satellite observations. This bias likely results in a reduced estimation of thermal stress, both at the surface and at reef depth. Because DHW is a cumulative metric, small temperature biases can lead to significant discrepancies in thermal stress estimates. This may, in turn, affect the identification and characterization of thermal refugia.

The estimation of the reef-depth Maximum Monthly Mean (MMM) also introduces uncertainty. In this study, the MMM was derived from data centered around 2017, whereas the standard NOAA climatology is based on an earlier reference period (1985–1990). This discrepancy implicitly assumes that the vertical thermal structure of the ocean has remained constant over time, which may not be valid. Furthermore, the MMM estimation relies on outputs from another numerical model (eReefs), which introduces an additional source of uncertainty. A more accurate approach would require in situ measurements of the temperature difference between the surface and reef depth, which are currently lacking in the study area.

The use of combined atmospheric forcings from two different datasets (BARRA2 and ERA5) may also introduce inconsistencies, particularly if differences exist in the representation of key variables such as surface heat fluxes.

Finally, the limited availability of observational data on the Queensland Plateau restricts the extent of model validation, especially for offshore processes.

In terms of perspectives, several improvements can be considered. Increasing the spatial resolution of the mesh, both near the GBR and around the reefs of the Queensland Plateau, would improve the representation of small-scale circulation and local hydrodynamic processes. The use of σ-layer vertical discretization, while challenging due to the need for bathymetry smoothing, would also enhance the representation of near-bottom processes and upwelling dynamics.

Coupling the hydrodynamic model with biological or ecological models would provide a more comprehensive understanding of the processes driving coral resilience and bleaching. In addition, extending the study to different climate scenarios would allow the assessment of the future evolution of thermal stress and the persistence of potential refugia under climate change conditions. Such analyses would provide valuable insights for the development of conservation and management strategies for coral reef ecosystems in the Queensland Plateau region.

Finally, given the key role of fine-scale bathymetric features in enhancing cold-water intrusions through tidal processes, an interesting perspective would be to investigate whether targeted modifications of local bathymetry could enhance such cooling mechanisms. The implementation of artificial underwater structures designed to promote upward transport of colder subsurface waters could potentially increase the thermal resilience of coral reefs. However, such approaches would require careful consideration of ecological impacts, hydrodynamic alterations, and habitat suitability to ensure that they do not negatively affect reef ecosystems.

5 Conclusion

This thesis investigated the local oceanographic processes that may mitigate thermal stress on coral reefs of the Queensland Plateau during the 2023–2024 marine heatwave. Using the three-dimensional baroclinic hydrodynamic model SLIM3D, the regional ocean dynamics and thermal conditions were simulated over the period from June 2023 to June 2024, and thermal stress was quantified using the Degree Heating Weeks metric computed at reef depth rather than at the sea surface.

The model was successfully validated against Argo float profiles and in situ ADCP observations, demonstrating a consistent representation of the regional thermohaline structure, vertical stratification, and large-scale circulation patterns including the South Equatorial Current, the North Caledonian Jet, and the East Australian Current. This validation provides confidence in the ability of the model to resolve the physical processes controlling reef-scale thermal variability.

The simulations reveal strong spatial heterogeneity in thermal stress across the Queensland Plateau, with significant differences between surface and reef-depth conditions at several reef systems. Two reefs were investigated in detail and found to benefit from distinct protective mechanisms operating at different spatial scales.

At Lihou Reef, reduced thermal stress in the southern region is primarily driven by mesoscale ocean circulation. The deflection of the North Caledonian Jet by Marion Reef generates a large persistent eddy that induces upwelling of cooler subsurface waters toward the reef, locally reducing sea surface temperatures and limiting heat stress accumulation. This mechanism highlights the role of regional-scale dynamics in shaping reef thermal environments, independently of local reef morphology.

At Diamond Reef, thermal mitigation is instead controlled by fine-scale local processes. The complex reef topography promotes tidal current acceleration through narrow passages, driving recurrent intrusions of cooler water into the lagoon at semi-diurnal frequency. These tidally driven exchanges generate strong thermal variability at reef depth and effectively limit the accumulation of Degree Heating Weeks within the identified refugia, while shallower and more exposed areas of the same reef experience significantly higher thermal stress.

Together, these findings indicate that thermal refugia in coral reefs on the Queensland Plateau cannot be explained by a single dominant mechanism. Rather, they result from the combined influence of regional ocean circulation and fine-scale bathymetric structures acting across multiple spatial scales. Importantly, this study demonstrates that sea surface temperature alone is not sufficient to represent thermal stress at reef depth, and that subsurface processes must be incorporated when evaluating coral reef vulnerability to marine heatwaves. These results have direct implications for the identification and protection of climate refugia and highlight the importance

of high-resolution three-dimensional hydrodynamic modelling as a tool for coral reef conservation in the context of ongoing climate change.

References

[1] Environmental Resources Information Network (ERIN). *Coral Sea Marine Park: Management plan 2018*. 2018. URL: https://australianmarineparks.gov.au/static/e7290288ff51dcc1604d8caa2679ea70/amp-document-coral-sea-management-plan-2018.pdf.

[2] John C. Andrews and Miles J. Furnas. "Subsurface intrusions of Coral Sea water into the central Great Barrier Reef—I. Structures and shelf-scale dynamics". In: *Continental Shelf Research* 6.4 (Jan. 1986), pp. 491–514. ISSN: 0278-4343. DOI: 10.1016/0278-4343(86)90020-8. URL: https://www.sciencedirect.com/science/article/pii/0278434386900208 (visited on 11/03/2025).

[3] R.J. Beaman. *AusBathyTopo (Great Barrier Reef) 30m 2017 - A regional-scale depth model (20170025C)*. en. 2020. DOI: 10.4225/25/5a207b36022d2. URL: https://pid.geoscience.gov.au/dataset/ga/115066 (visited on 09/11/2025).

[4] Christian Betzler, Thomas C. Brachert, and Dick Kroon. "Role of climate in partial drowning of the Queensland Plateau carbonate platform (northeastern Australia)". In: *Marine Geology* 123.1 (Mar. 1995), pp. 11–32. ISSN: 0025-3227. DOI: 10.1016/0025-3227(95)80002-S. URL: https://www.sciencedirect.com/science/article/pii/002532279580002S (visited on 02/03/2026).

[5] Bureau of Meteorology. *Atmospheric high-resolution reanalysis (BARRA)*. Accessed: 2026-05-14. 2025. URL: https://www.bom.gov.au/government-and-industry/research-and-development/research-and-development-projects/atmospheric-reanalysis.

[6] Bureau of Meteorology. *Atmospheric High-Resolution Reanalysis for Australia (BARRA)*. Accessed: 2026-05-29. n.d. URL: https://www.bom.gov.au/government-and-industry/research-and-development/research-and-development-projects/atmospheric-reanalysis.

[7] Copernicus Climate Change Service (C3S). *ERA5 pressure-levels daily statistics*. Accessed: 2026-05-29. n.d. URL: https://cds.climate.copernicus.eu/datasets/derived-era5-pressure-levels-daily-statistics?tab=overview.

[8] Robert Costanza et al. "Changes in the global value of ecosystem services". In: *Global Environmental Change* 26 (May 2014), pp. 152–158. ISSN: 0959-3780. DOI: 10.1016/j.gloenvcha.2014.04.002. URL: https://www.sciencedirect.com/science/article/pii/S0959378014000685 (visited on 10/06/2025).

[9] Philippe Delandmeter. "Discontinuous Galerkin finite element modelling of geophysical and environmental flows". In: 2017. URL: https://api.semanticscholar.org/CorpusID:125595802.

[10] Adele M. Dixon et al. "Future loss of local-scale thermal refugia in coral reef ecosystems". en. In: *PLOS Climate* 1.2 (Feb. 2022). Publisher: Public Library of Science, e0000004. ISSN: 2767-3200. DOI: 10.1371/journal.pclm.0000004. URL: https://journals.plos.org/climate/article?id=10.1371/journal.pclm.0000004 (visited on 10/22/2025).

[11] A. E. Douglas. "Coral bleaching—how and why?" In: *Marine Pollution Bulletin* 46.4 (Apr. 2003), pp. 385–392. ISSN: 0025-326X. DOI: 10.1016/S0025-326X(03)00037-7. URL: https://www.sciencedirect.com/science/article/pii/S0025326X03000377 (visited on 11/03/2025).

[12] C. Mark Eakin et al. "Caribbean Corals in Crisis: Record Thermal Stress, Bleaching, and Mortality in 2005". en. In: *PLOS ONE* 5.11 (Nov. 2010). Publisher: Public Library of Science, e13969. ISSN: 1932-6203. DOI: 10.1371/journal.pone.0013969. URL: https://journals.plos.org/plosone/article?id=10.1371/journal.pone.0013969 (visited on 11/04/2025).

[13] Mattias Van Eetvelt. "Simplified mathematical description of SLIM3D". In: 2026.

[14] "Examples of calculation methods for flow and mixing in stratified fluids". en. In: *Journal of Geophysical Research: Oceans* 92.C5 (1987). _eprint: https://agupubs.onlinelibrary.w pp. 5305–5328. ISSN: 2156-2202. DOI: 10.1029/JC092iC05p05305. URL: https://onlinelibrary.wiley.com/doi/abs/10.1029/JC092iC05p05305 (visited on 03/02/2026).

[15] *Great Barrier Reef World Heritage Area - DCCEEW*. URL: https://www.dcceew.gov.au/parks-heritage/great-barrier-reef/world-heritage (visited on 10/03/2025).

[16] B. Henderson-Sellers. "A new formula for latent heat of vaporization of water as a function of temperature". en. In: *Quarterly Journal of the Royal Meteorological Society* 110.466 (1984). _eprint: https://rmets.onlinelibrary.wiley.com/doi/pdf/10.1002/qj.497 pp. 1186–1190. ISSN: 1477-870X. DOI: 10.1002/qj.49711046626. URL: https://onlinelibrary.wiley.com/doi/abs/10.1002/qj.49711046626 (visited on 03/02/2026).

[17] Ove Hoegh-Guldberg. "Climate change, coral bleaching and the future of the world's coral reefs". In: *Marine & Freshwater Research* 50.8 (Nov. 1999), pp. 839–866. ISSN: 1323-1650. DOI: 10.1071/MF99078. URL: https://doi.org/10.1071/MF99078 (visited on 11/03/2025).

[18] Andrew Hoey. “Coral sea marine park coral reef health survey 2023-24”. en. In: (). URL: https://australianmarineparks.gov.au/science/scientific-publications/coral-sea-marine-park-coral-reef-health-survey-2023-and-2024/.

[19] Professor Andrew Hoey. *Assessment of the 2024 marine heatwave on five reefs in the central Coral Sea Marine Park*. en. James Cook University, Townsville QLD 48110, 2024. URL: https://australianmarineparks.gov.au/science/scientific-publications/assessment-2024-marine-heatwave-on-five-reefs-central-coral-sea-marine-park/ (visited on 11/10/2025).

[20] Terry P. Hughes et al. “Global warming and recurrent mass bleaching of corals”. en. In: *Nature* 543.7645 (Mar. 2017). Publisher: Nature Publishing Group, pp. 373–377. ISSN: 1476-4687. DOI: 10.1038/nature21707. URL: https://www.nature.com/articles/nature21707 (visited on 11/03/2025).

[21] David R. Jackett et al. “Algorithms for Density, Potential Temperature, Conservative Temperature, and the Freezing Temperature of Seawater”. In: *Journal of Atmospheric and Oceanic Technology* 23.12 (2006), pp. 1709–1728. DOI: 10.1175/JTECH1946.1. URL: https://journals.ametsoc.org/view/journals/atot/23/12/jtech1946_1.xml.

[22] William Leggat et al. “Experiment Degree Heating Week (eDHW) as a novel metric to reconcile and validate past and future global coral bleaching studies”. In: *Journal of Environmental Management* 301 (Jan. 2022), p. 113919. ISSN: 0301-4797. DOI: 10.1016/j.jenvman.2021.113919. URL: https://www.sciencedirect.com/science/article/pii/S0301479721019812 (visited on 11/05/2025).

[23] Gang Liu et al. “Predicting Heat Stress to Inform Reef Management: NOAA Coral Reef Watch’s 4-Month Coral Bleaching Outlook”. English. In: *Frontiers in Marine Science* 5 (Mar. 2018). Publisher: Frontiers. ISSN: 2296-7745. DOI: 10.3389/fmars.2018.00057. URL: https://www.frontiersin.org/journals/marine-science/articles/10.3389/fmars.2018.00057/full (visited on 11/04/2025).

[24] Gang Liu et al. “Reef-Scale Thermal Stress Monitoring of Coral Ecosystems: New 5-km Global Products from NOAA Coral Reef Watch”. en. In: *Remote Sensing* 6.11 (Nov. 2014). Company: Multidisciplinary Digital Publishing Institute Distributor: Multidisciplinary Digital Publishing Institute Institution: Multidisciplinary Digital Publishing Institute Label: Multidisciplinary Digital Publishing Institute Publisher: publisher, pp. 11579–11606. ISSN: 2072-4292. DOI: 10.3390/rs61111579. URL: https://www.mdpi.com/2072-4292/6/11/11579 (visited on 11/04/2025).

[25] J. M. Lough and M. J. H. van Oppen. "Introduction: Coral Bleaching–Patterns, Processes, Causes and Consequences". en. In: *Coral Bleaching: Patterns, Processes, Causes and Consequences*. Ed. by Madeleine J. H. van Oppen and Janice M. Lough. Cham: Springer International Publishing, 2018, pp. 1–8. ISBN: 978-3-319-75393-5. DOI: 10.1007/978-3-319-75393-5_1. URL: https://doi.org/10.1007/978-3-319-75393-5_1 (visited on 11/03/2025).

[26] Donna Lu. *Certain corals can recover from bleaching during prolonged heatwaves*. en-US. URL: https://www.newscientist.com/article/2262056-certain-corals-can-recover-from-bleaching-during-prolonged-heatwaves/ (visited on 11/03/2025).

[27] John Marshall and Alan Plumb. "Circulation of the Atmosphere and Ocean: an introductory text". In: *Massachusetts Institute of Technology* (2007).

[28] Fredrik Moberg and Carl Folke. "Ecological goods and services of coral reef ecosystems". In: *Ecological Economics* 29.2 (May 1999), pp. 215–233. ISSN: 0921-8009. DOI: 10.1016/S0921-8009(99)00009-9. URL: https://www.sciencedirect.com/science/article/pii/S0921800999000099 (visited on 10/02/2025).

[29] L. Muscatine and James W. Porter. "Reef Corals: Mutualistic Symbioses Adapted to Nutrient-Poor Environments". In: *BioScience* 27.7 (1977). Publisher: [American Institute of Biological Sciences, Oxford University Press], pp. 454–460. ISSN: 0006-3568. DOI: 10.2307/1297526. URL: https://www.jstor.org/stable/1297526 (visited on 11/03/2025).

[30] National Oceanic and Atmospheric Administration. *Argo Program*. Accessed: 2026-05-12. 2026. URL: https://globalocean.noaa.gov/research/argo-program/.

[31] NOAA Coral Reef Watch. *Coral Reef Watch Daily 5 km Global Products*. Accessed: 2026-05-25. 2024. URL: https://coralreefwatch.noaa.gov/product/5km/index_5km_composite.php.

[32] *NOAA Coral Reef Watch Version 3.1 5-km Product Climatology Description*. Accessed: 2026-05-23. 2026. URL: https://coralreefwatch.noaa.gov/product/5km/description_climatology.php.

[33] *Ocean Wiki - Ekman Transport*. https://oceanwiki.ethz.ch/doku.php?id=lecture7:ekman. Accessed: 2025-11-03. (Visited on 11/03/2025).

[34] Howard T. Odum and Eugene P. Odum. "Trophic Structure and Productivity of a Windward Coral Reef Community on Eniwetok Atoll". In: *Ecological Monographs* 25.3 (1955). Publisher: [Wiley, Ecological Society of America], pp. 291–320. ISSN: 0012-9615. DOI: 10.2307/1943285. URL: https://www.jstor.org/stable/1943285 (visited on 10/02/2025).

[35] Akira Okubo. “Oceanic diffusion diagrams”. In: *Deep Sea Research and Oceanographic Abstracts* 18.8 (1971), pp. 789–802. ISSN: 0011-7471. DOI: https://doi.org/10.1016/0011-7471(71)90046-5. URL: https://www.sciencedirect.com/science/article/pii/0011747171900465.

[36] *SLIM3D*. https://www.slim-ocean.be/index.php/slim3d/. Accessed: 2025-11-10.

[37] J. SMAGORINSKY. “GENERAL CIRCULATION EXPERIMENTS WITH THE PRIMITIVE EQUATIONS: I. THE BASIC EXPERIMENT”. In: *Monthly Weather Review* 91.3 (1963), pp. 99–164. DOI: 10.1175/1520-0493(1963)091<0099:GCEWTP>2.3.CO;2. URL: https://journals.ametsoc.org/view/journals/mwre/91/3/1520-0493_1963_091_0099_gcewtp_2_3_co_2.xml.

[38] S. D. Smith and E. G. Banke. “Variation of the sea surface drag coefficient with wind speed”. en. In: *Quarterly Journal of the Royal Meteorological Society* 101.429 (1975). ISSN: 1477-870X. DOI: 10.1002/qj.49710142920. URL: https://onlinelibrary.wiley.com/doi/abs/10.1002/qj.49710142920 (visited on 03/02/2026).

[39] Noga Stambler. “Zooxanthellae: The Yellow Symbionts Inside Animals”. en. In: *Coral Reefs: An Ecosystem in Transition*. Ed. by Zvy Dubinsky and Noga Stambler. Dordrecht: Springer Netherlands, 2011, pp. 87–106. ISBN: 978-94-007-0114-4. DOI: 10.1007/978-94-007-0114-4_7. URL: https://doi.org/10.1007/978-94-007-0114-4_7 (visited on 11/03/2025).

[40] Chaojiao Sun et al. “Climate refugia in the Great Barrier Reef may endure into the future”. In: *Science Advances* 10.48 (Nov. 2024). Publisher: American Association for the Advancement of Science, eado6884. DOI: 10.1126/sciadv.ado6884. URL: https://www.science.org/doi/10.1126/sciadv.ado6884 (visited on 11/03/2025).

[41] Rory O. R. Y. Thompson and T. J. Golding. “Tidally induced ‘upwelling’ by the Great Barrier Reef”. en. In: *Journal of Geophysical Research: Oceans* 86.C7 (1981). _eprint: https://agupubs.onlinelibrary.wiley.com/doi/pdf/10.1029/JC086iC07p06517, pp. 6517–6521. ISSN: 2156-2202. DOI: 10.1029/JC086iC07p06517. URL: https://onlinelibrary.wiley.com/doi/abs/10.1029/JC086iC07p06517 (visited on 10/22/2025).

[42] UCLouvain. *SLIM3D and numerical issues*. Accessed: 2026-05-29. n.d. URL: https://forge.uclouvain.be/slim-enge/scripts/-/wikis/SLIM3D-and-numerical-issues.

[43] R. M. Venegas, T. Oliver, G. Liu, et al. “The Rarity of Depth Refugia from Coral Bleaching Heat Stress in the Western and Central Pacific Islands”. In: *Scientific Reports* 9 (2019), p. 19710. DOI: 10.1038/s41598-019-56232-1. URL: https://doi.org/10.1038/s41598-019-56232-1.

[44] S. J. Weeks et al. “The Capricorn Eddy: a prominent driver of the ecology and future of the southern Great Barrier Reef”. en. In: *Coral Reefs* 29.4 (Dec. 2010), pp. 975–985. ISSN: 1432-0975. DOI: 10.1007/s00338-010-0644-z. URL: https://doi.org/10.1007/s00338-010-0644-z (visited on 11/03/2025).

[45] *What Is Coral Bleaching? Causes, Impacts & Action for the Great Barrier Reef.* en. URL: https://www.barrierreef.org/the-reef/threats/coral-bleaching (visited on 11/03/2025).

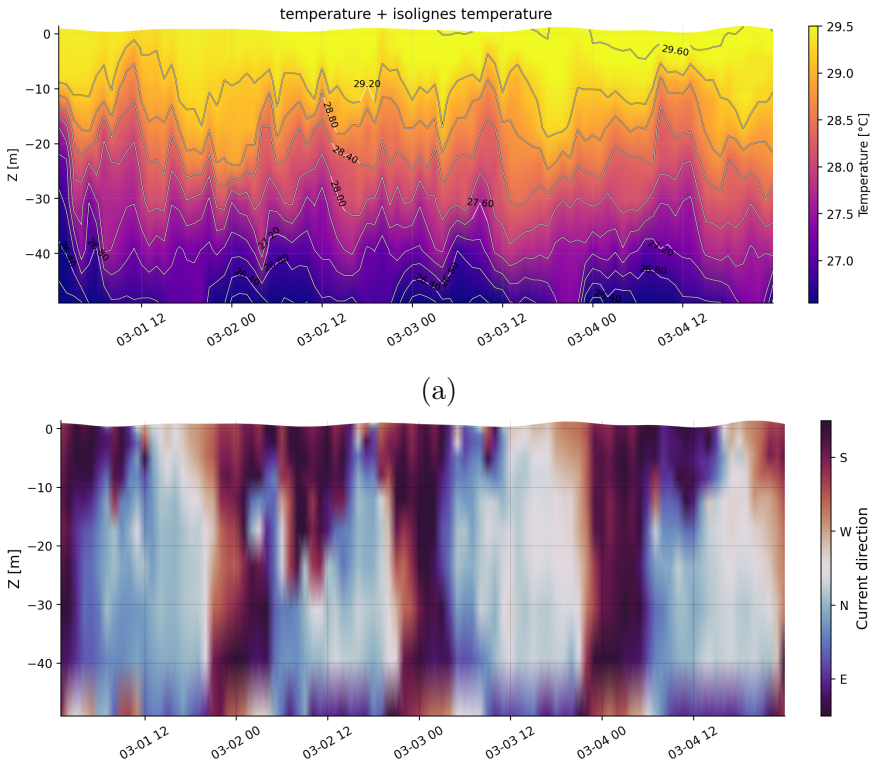
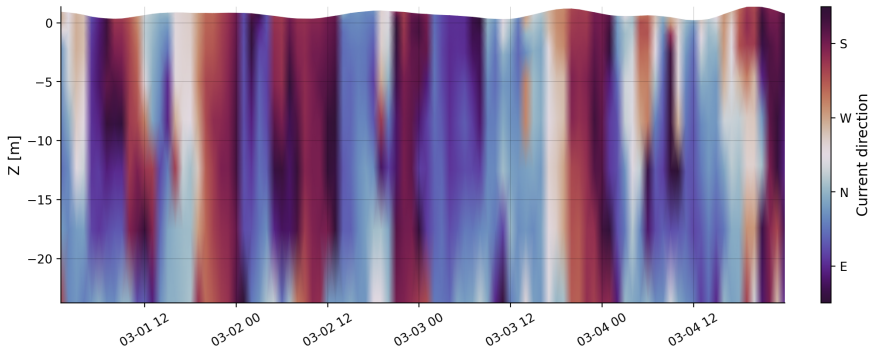


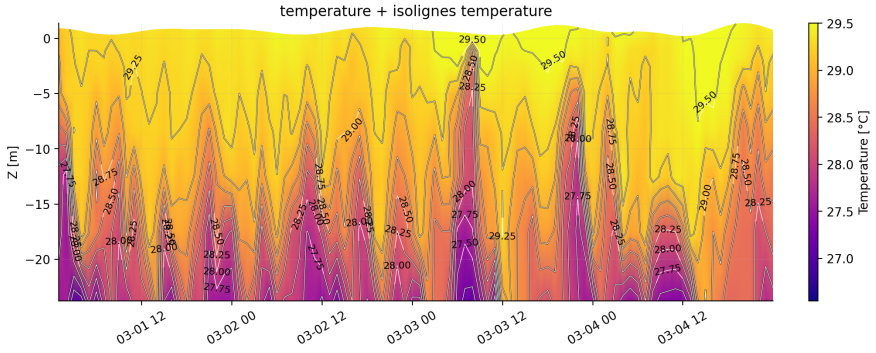
Figure 43: Vertical profile time series of (a) temperature and (b) current direction at the northern refugium (Fig. 37) during the period from January 1 to May 1, 2024. These figures highlight the intrusion of cold water into the Diamond lagoon following a 12-hour cycle linked to the tidal regime in this area.

A Diamond Reef refigua

This appendix present the results obtained for the two other identified refugia on the Diamond Reef.



(a)



(b)

Figure 44: Vertical profile time series of (a) temperature and (b) current direction at the eastern refugium (Fig. 37) during the period from January 1 to May 1, 2024. These figures highlight the intrusion of cold water into the Diamond lagoon following a 12-hour cycle linked to the tidal regime in this area.

B Analysis of tidal influence on seabed temperature

This appendix describes the methodology used to analyse the relationship between seabed temperature variability and tidal forcing. Although this analysis is not the primary focus of the thesis, it provides useful insights into the physical mechanisms controlling thermal variability at reef depth.

B.1 Dominant frequency estimation

To characterise vertical variability in the water column, the dominant frequency of a given variable (e.g. temperature) is computed independently at each depth level.

Given a time series $x(t)$ at a fixed depth, the frequency spectrum is estimated using Welch's method. This approach consists in dividing the signal into overlapping segments, computing the Fourier transform of each segment, and averaging the resulting power spectral densities (PSD). This reduces variance compared to a standard Fourier transform.

The PSD is expressed as a function of frequency f, and the dominant frequency $f_{\max}$ is defined as:

$$f_{\max} = \arg\max_{f>0} \mathrm{PSD}(f) \tag{1}$$

The corresponding dominant period is then given by:

$$T = \frac{1}{f_{\max}} \tag{2}$$

This procedure is repeated at all depths, producing a vertical profile of dominant periods, which allows identification of differences between surface and subsurface variability regimes.

B.2 Tidal signal and seabed temperature

To investigate the interaction between tides and seabed temperature, a proxy for tidal forcing is constructed using the free surface elevation $\eta(t)$.

Two alternative definitions are used in the model:

- the surface elevation, defined as the maximum vertical coordinate of the water column,
- or the total water column thickness.

The time series of seabed temperature $T_b(t)$ (bottom layer) and tidal elevation $\eta(t)$ are first detrended by removing their mean:

$$T_b'(t) = T_b(t) - \overline{T_b}, \quad \eta'(t) = \eta(t) - \overline{\eta} \tag{3}$$

B.3 Spectral analysis

The frequency content of both seabed temperature and tidal elevation is analysed using Welch's method, similarly to the dominant frequency calculation.

The resulting power spectral densities are expressed as functions of period, allowing direct identification of characteristic time scales. In particular, tidal processes are expected to appear at periods corresponding to the main tidal constituents:

- semi-diurnal tides ($\sim$ 12.4 hours),
- diurnal tides ($\sim$ 24 hours).

Comparing the spectra of temperature and tidal elevation allows assessing the extent to which tidal forcing contributes to temperature variability.

B.4 Interpretation

This combined analysis provides complementary information:

- dominant frequency profiles highlight differences between surface and bottom variability,
- spectral analysis identifies the contribution of tidal frequencies to temperature variability.

Together, these tools allow a qualitative assessment of the role of tidal processes in modulating seabed temperature and, consequently, thermal stress at reef depth.

UNIVERSITÉ CATHOLIQUE DE LOUVAIN
École polytechnique de Louvain
Rue Archimède, 1 bte L6.11.01, 1348 Louvain-la-Neuve, Belgique | **www.uclouvain.be/epl**